

Evidential Neural Radiance Fields

Ruxiao Duan
Yale University

ruxiao.duan@yale.edu

Alex Wong
Yale University

alex.wong@yale.edu

Abstract

Understanding sources of uncertainty is fundamental to trustworthy three-dimensional scene modeling. While recent advances in neural radiance fields (NeRFs) achieve impressive accuracy in scene reconstruction and novel view synthesis, the lack of uncertainty estimation significantly limits their deployment in safety-critical settings. Existing uncertainty quantification methods for NeRFs fail to capture both aleatoric and epistemic uncertainty. Among those that do quantify one or the other, many of them either compromise rendering quality or incur significant computational overhead to obtain uncertainty estimates. To address these issues, we introduce Evidential Neural Radiance Fields, a probabilistic approach that seamlessly integrates with the NeRF rendering process and enables direct quantification of both aleatoric and epistemic uncertainty from a single forward pass. We compare multiple uncertainty quantification methods on three standardized benchmarks, where our approach demonstrates state-of-the-art scene reconstruction fidelity and uncertainty estimation quality.

1. Introduction

Predictive uncertainty of deep neural networks originates from two different sources, data and model, and the two types of uncertainty are respectively referred to as aleatoric uncertainty (AU) and epistemic uncertainty (EU) [14, 17]. Aleatoric (data) uncertainty stems from intrinsic randomness of the data generation process, while epistemic (model) uncertainty arises from model’s lack of knowledge [9, 12]. Understanding both types of predictive uncertainty is essential for building models that are not only accurate but also reliable and explainable under various conditions.

Neural radiance fields (NeRFs) [24] have achieved remarkable performance in three-dimensional (3D) scene reconstruction and novel view synthesis, yet their incapability of quantifying predictive uncertainty poses significant challenges for their broader adoption in safety-critical domains such as autonomous driving [11], medical imaging [44], and robotics [43], where precise and prompt quantification of

predictive uncertainty remains crucial.

We consider an essential but overlooked research question: *How should a NeRF report what it does not know (epistemic uncertainty) versus what the data cannot resolve (aleatoric uncertainty), without sacrificing rendering fidelity or speed?* Existing uncertainty quantification (UQ) methods for NeRFs generally fall into three categories: closed-form likelihood models, which are unable to capture epistemic uncertainty [22, 28, 34, 35], Bayesian methods, which typically necessitate sampling during inference [7, 36, 37], and ensemble approaches, which require training multiple models [21, 40]. None of these methods quantifies both types of uncertainty with a single forward pass, and many of them have to sacrifice prediction accuracy to obtain uncertainty estimates.

Among the existing uncertainty quantification approaches, a normal-distribution-based method [17] treat each output as distributional parameters, where its mean represents the prediction and variance encodes the uncertainty. This formulation and its variants have been widely adopted in not only NeRFs [22, 28, 29] but also other radiance field frameworks such as DVGO [38, 39] and Gaussian Splatting [18, 20]. While computationally efficient, this paradigm inherently models only aleatoric uncertainty and fails to account for epistemic uncertainty.

To address these limitations of existing work, we propose Evidential Neural Radiance Fields (Evidential NeRFs), a probabilistic framework to quantify both aleatoric and epistemic uncertainty of NeRFs through a single forward pass. Our method extends the probabilistic formulation of radiance modeling by treating the predicted mean and variance of pixel radiance themselves as random variables governed by a higher-order evidential distribution, yielding closed-form predictive uncertainties through the NeRF rendering process. Unlike prior evidential deep learning methods [1, 33], which regress evidential distribution parameters, we adapt evidential reasoning to the volumetric structure of NeRFs, enabling them to predict aleatoric and epistemic uncertainties directly instead of having to reformulate them from evidential parameters.

Beyond the technical limitations of existing approaches

– which we address with Evidential NeRF – we also observed that current uncertainty quantification benchmarks lack standardization. Methods are often evaluated using different architectures, data splits, and training setups, making direct comparisons difficult. To mitigate these confounding factors, we establish a new benchmark designed to isolate and evaluate the UQ methods themselves. We reproduce recent approaches on the nerfacto architecture and run each method three times independently, reporting averaged metrics. Under this standardized evaluation, our method consistently ranks within the top three across all metrics, if not the first. The remaining top-performing methods are ensemble-based, which incur substantial computational cost and are unsuitable for real-time applications. In contrast, our approach is the second-fastest overall; we are only 0.04 FPS slower than the fastest method, but deliver significantly better performance across all metrics.

Our contributions can be summarized as follows.

- We are the first to present a framework for neural radiance fields to quantify both aleatoric and epistemic uncertainties in 3D scene reconstructions.
- We provide detailed mathematical derivations showing how aleatoric and epistemic uncertainties can be propagated from voxels to pixels under proper independence assumptions, enabling seamless integration of evidential deep learning with the volumetric rendering paradigm.
- We establish a standardized benchmark for faithful comparison of UQ methods for NeRFs, ensuring experimental fidelity and reproducibility by releasing codebase.

2. Related Work

Neural radiance fields. NeRFs [24] represent a 3D scene as a plenoptic function which can be learned from a sparse set of input views. Realized as a deep neural network, the plenoptic function maps spatial locations and viewing directions to their volume densities and radiance. NeRFs produce high-fidelity reconstructions and photorealistic novel view renderings, and numerous variants in architectures, loss functions, and sampling strategies have been proposed to further improve the model’s training efficiency, inference speed, and rendering quality [2–6, 8, 13, 15, 26, 27, 42, 45].

Uncertainty quantification for NeRFs. UQ methods for NeRFs generally follow three schools of thought.

First, closed-form likelihood models. NeRF-W [22] and ActiveNeRF [28] follow the same probabilistic framework in [17] to model ray colors by normal distributions. MixNeRF [35] and FlipNeRF [34], though not proposed as UQ methods, model ray colors by mixtures of Laplace distributions to represent the multimodal nature of radiance. These approaches employ closed-form probabilistic distributions to model pixel colors, enabling efficient training and uncertainty inference, but overlooking epistemic uncertainty, due to the deterministic nature of the selected distributions.

Second, Bayesian methods. Monte Carlo dropout [7] estimates epistemic uncertainty by interpreting dropout as variational inference and performing multiple stochastic forward passes at test time. S-NeRF [36] and CF-NeRF [37] learn a probability distribution over all the possible radiance fields and approximate the posterior distribution with stochastic variational inference [19] and conditional normalizing flows [30]. BayesRays [10] derives a volumetric epistemic uncertainty field of a pre-trained NeRF model based on spatial perturbations and Bayesian Laplace approximation [31]. While these approaches provide epistemic uncertainty estimates, they typically incur significant computational overhead at inference, either due to repeated sampling or post-hoc learning of uncertainty fields.

Third, ensemble methods. Deep ensembles [21] estimate epistemic uncertainty by training multiple models independently and measuring their prediction variance during inference. Density-aware NeRF Ensembles (DANE) [40] further incorporates a density-based epistemic term that captures uncertainty in scene geometry and appearance, which is added to the uncertainty estimated by standard ensembles. Ensemble-based methods impose the most significant computation and memory overheads, as each model must be trained, stored, and separately evaluated during inference.

Evidential deep learning. Based on the theory of subjective logic [16], evidential deep learning (EDL) [33] is first introduced for classification uncertainty quantification based on a single network and later extended to regression [1]. EDL considers model learning as a process of evidence collection, in which each training sample adds support to a higher-order evidential distribution, which is a Dirichlet distribution for classification and a Normal Inverse-Gamma distribution for regression [1, 33]. The probability distribution from which predictions are drawn is assumed to have random parameters sampled from the evidential distribution, and the aleatoric and epistemic predictive uncertainties can be directly obtained by a single forward propagation. Though effective in standard regression, EDL is not naively compatible with NeRF learning paradigm due to its hierarchical volumetric formulation: As NeRFs receive supervision after volumetric rendering, evidential parameters tied to voxel-level predictions cannot be learned directly from pixel-level observations.

3. Preliminaries

Neural radiance fields. NeRF learns a continuous scene representation function f by a multilayer perceptron that maps a pair of spatial location $\mathbf{x}_i \in \mathbb{R}^3$ and unit viewing direction $\mathbf{d} \in \mathbb{R}^3$ to its corresponding view-independent volume density $\rho_i > 0$ and directional emitted radiance $\mathbf{c}_i \in [0, 1]^3$ in RGB color. For notational simplicity, con-

sider a scalar color channel $c_i \in [0, 1]$. NeRF predicts

$$c_i, \rho_i = f(\mathbf{x}_i, \mathbf{d}), \quad (1)$$

where ρ_i is produced by a density network depending solely on \mathbf{x}_i . The pixel color of a ray $\mathbf{r}(t) = \mathbf{o} + t\mathbf{d}$ defined by a camera center \mathbf{o} and a viewing direction \mathbf{d} is derived by first sampling N voxels $\{\mathbf{r}(t_i)\}_{i=1}^N$ along the ray and then computing the weighted sum of voxel colors via the discretized volume rendering equation $c = \sum_{i=1}^N w_i c_i$, where $w_i = \exp\left(-\sum_{j=1}^{i-1} \rho_j \delta_j\right) (1 - \exp(-\rho_i \delta_i))$ is the weight of the i -th voxel and $\delta_i = t_{i+1} - t_i$ denotes the distance between two adjacent voxels.

Normal distribution for radiance modeling. Previous works [22, 28] propose to model each voxel color c_i by a normal distribution

$$c_i \mid \mu_i, \sigma_i^2 \sim \mathcal{N}(\mu_i, \sigma_i^2), \quad (2)$$

with mean $\mu_i \in [0, 1]$ and variance $\sigma_i^2 > 0$ predicted by

$$\mu_i, (\rho_i, \sigma_i^2) = f(\mathbf{x}_i, \mathbf{d}), \quad (3)$$

where ρ_i and σ_i^2 are put into one parenthesis to denote they are outputs of the view-independent network. As the pixel color c is the weighted sum of voxel colors c_i 's, c also follows a normal distribution assuming voxel independence:

$$c \mid \mu, \sigma^2 \sim \mathcal{N}(\mu, \sigma^2), \quad (4)$$

where $\mu := \sum_{i=1}^N w_i \mu_i$ is the mean (prediction) and $\sigma^2 := \sum_{i=1}^N w_i^2 \sigma_i^2$ is the variance (uncertainty) of pixel color. While adjacent voxels in practice exhibit statistical dependence in radiance, the independence assumption is a common and effective simplification to enable tractable aggregation of voxel uncertainties into the pixel level. Though efficient, this method only captures aleatoric uncertainty.

4. Method

Based on Equations (2) and (4), we establish an evidential probabilistic framework for radiance modeling by taking a step further to assume random conditional mean and variance. Different from conventional EDL approaches which train the model to predict evidential parameters, we instead let the model predict aleatoric and epistemic uncertainties directly (Section 4.1), and then propagate the uncertainties from voxels to pixels compatible to the volumetric rendering paradigm of NeRFs (Section 4.2). Then the evidential distribution can be reformulated from the rendered color and uncertainties (Section 4.3) and learned at the pixel level where supervision is available (Section 4.4).

4.1. Voxel-level Probabilistic Radiance Modeling

Supposing Equation (2) continues to hold, we further treat the conditional mean and variance of voxel radiance as random variables instead of point estimates, i.e., $(\mu_i, \sigma_i^2) \sim \pi_i$

where π_i is some unknown probability distribution without being restricted to any parametric family. This assumption is crucial, as committing to a specific closed-form distribution would make it nontrivial to construct the desired pixel-level evidential distribution in Equation (14). Under this formulation, the predictive mean, total, aleatoric, and epistemic uncertainty of the voxel color c_i are defined as

$$\bar{c}_i := \mathbb{E}[c_i] = \mathbb{E}[\mathbb{E}[c_i \mid \mu_i, \sigma_i^2]] = \mathbb{E}[\mu_i], \quad (5)$$

$$U_i := \text{Var}[c_i] = U_i^{\text{alea}} + U_i^{\text{epis}}, \quad (6)$$

$$U_i^{\text{alea}} := \mathbb{E}[\text{Var}[c_i \mid \mu_i, \sigma_i^2]] = \mathbb{E}[\sigma_i^2], \quad (7)$$

$$U_i^{\text{epis}} := \text{Var}[\mathbb{E}[c_i \mid \mu_i, \sigma_i^2]] = \text{Var}[\mu_i]. \quad (8)$$

Note: The classical assumption that μ_i and σ_i^2 are point estimates corresponds to the special case where π_i is a degenerate distribution with a Dirac delta density function concentrated at fixed values of $\hat{\mu}_i$ and $\hat{\sigma}_i^2$ and the uncertainties above are thereby reduced to $U_i^{\text{alea}} = \mathbb{E}[\sigma_i^2] = \hat{\sigma}_i^2$ and $U_i^{\text{epis}} = \text{Var}[\mu_i] = 0$, in which case only aleatoric uncertainty can be captured.

An Evidential NeRF model predicts

$$\bar{c}_i, (\rho_i, U_i^{\text{alea}}, U_i^{\text{epis}}, \tilde{\alpha}_i) = f(\mathbf{x}_i, \mathbf{d}), \quad (9)$$

where $\bar{c}_i \in [0, 1]$ is the voxel's mean color, $\rho_i > 0$ is the volume density, $U_i^{\text{alea}} > 0$ and $U_i^{\text{epis}} > 0$ are aleatoric and epistemic uncertainties, and $\tilde{\alpha}_i > 0$ is a positive shape score which will later be used to derive a pixel-level shape parameter α in Section 4.3. We apply sigmoid activation to predict \bar{c}_i as in original NeRF and softplus activation for all other parameters to enforce range restrictions. All uncertainty-related parameters are predicted by the view-independent density network following [22, 28]. The model architecture remains unchanged, except the three additional output neurons of the density network to predict $(U_i^{\text{alea}}, U_i^{\text{epis}}, \tilde{\alpha}_i)$.

4.2. Propagation from Voxels to Pixels

Let the set of conditional means and variances of all voxel colors along a ray be $\boldsymbol{\theta} := \{(\mu_i, \sigma_i^2)\}_{i=1}^N$, which fully specifies the conditional distribution of the ray color c . Under this setting, the pixel's predictive mean color, total, aleatoric, and epistemic uncertainties are defined as

$$\bar{c} := \mathbb{E}[c], \quad U := \text{Var}[c], \quad (10)$$

$$U^{\text{alea}} := \mathbb{E}[\text{Var}[c \mid \boldsymbol{\theta}]], \quad U^{\text{epis}} := \text{Var}[\mathbb{E}[c \mid \boldsymbol{\theta}]]. \quad (11)$$

With the voxel-level predictions from the Evidential NeRF model in Equation (9) and the assumptions that the voxel colors are independent and conditionally independent

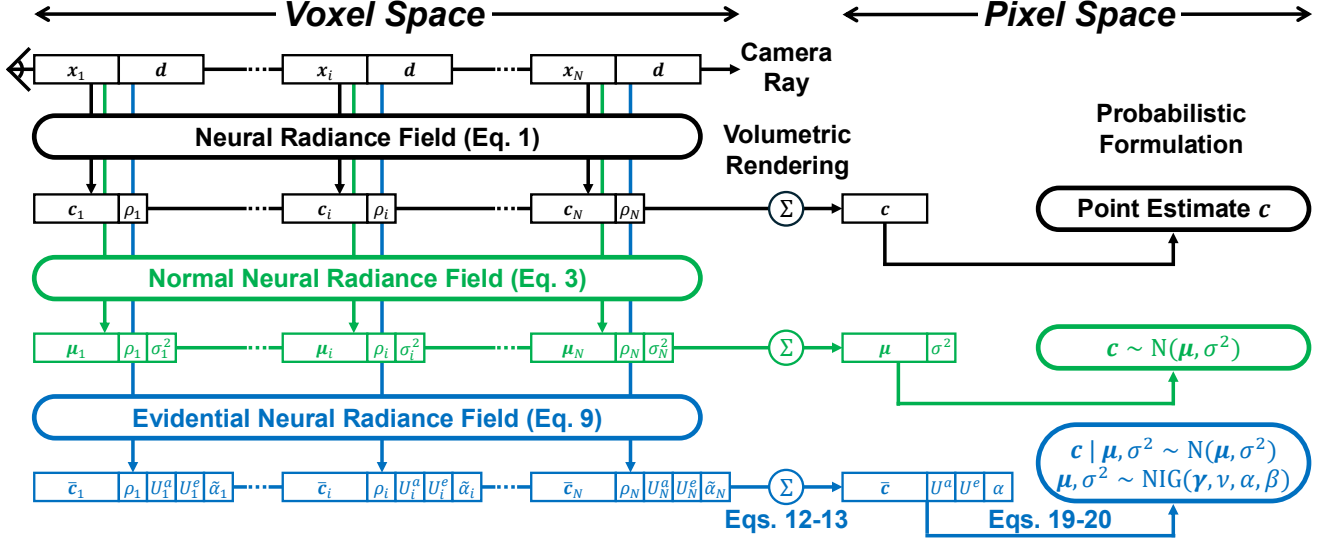


Figure 1. Evolution of NeRF pipeline across three levels of probabilistic formulations. N voxels sampled along the camera ray give N pairs of spatial location and view direction, which are passed to the NeRF model for prediction. Level 1: Vanilla NeRF predicts only voxel density and color, resulting in a point estimate of pixel color without any uncertainty estimate. Level 2: Normal NeRF assumes the voxel and pixel colors follow normal distributions, quantifying aleatoric uncertainty of rendered color. Level 3: Evidential NeRF assumes the pixel color has random mean and variance following an evidential distribution, quantifying both aleatoric and epistemic uncertainties.

given θ , the pixel color and uncertainties can be derived as

$$\bar{c} = \sum_{i=1}^N w_i \bar{c}_i, \quad U = \sum_{i=1}^N w_i^2 U_i, \quad (12)$$

$$U^{\text{alea}} = \sum_{i=1}^N w_i^2 U_i^{\text{alea}}, \quad U^{\text{epis}} = \sum_{i=1}^N w_i^2 U_i^{\text{epis}}. \quad (13)$$

In other words, pixel-level aleatoric and epistemic uncertainties can be obtained as weighted sums of their voxel-level counterparts, where the weights are equal to the squared weights for color volumetric rendering. Detailed proofs are provided in the supplementary Section 7.

4.3. Pixel-level Probabilistic Radiance Modeling

Now we introduce the probabilistic model for pixel colors. Recall that $\mu = \sum_{i=1}^N w_i \mu_i$ and $\sigma^2 = \sum_{i=1}^N w_i^2 \sigma_i^2$ represent the conditional mean and variance of the pixel color c in Equation (4). To quantify aleatoric and epistemic uncertainties of a pixel color in closed form, we model (μ, σ^2) by a normal-inverse-gamma (NIG) distribution

$$\mu, \sigma^2 \sim \text{NIG}(\gamma, \nu, \alpha, \beta), \quad (14)$$

or equivalently, $\mu | \sigma^2 \sim \mathcal{N}(\gamma, \sigma^2/\nu)$ and $\sigma^2 \sim \Gamma^{-1}(\alpha, \beta)$, where $\gamma \in \mathbb{R}$, $\nu > 0$, and $\Gamma^{-1}(\alpha, \beta)$ denotes an inverse-gamma distribution with shape $\alpha > 1$ and scale $\beta > 0$. Consider each pixel color c as being generated through a hierarchical sampling process: Given the higher-order evidential distribution $\text{NIG}(\gamma, \nu, \alpha, \beta)$, drawing a sample (μ, σ^2) from it yields an instance of lower-order normal distribution $\mathcal{N}(\mu, \sigma^2)$, from which the pixel color c is sampled.

With this formulation, the pixel color's predictive mean, total, aleatoric, and epistemic uncertainties can be directly expressed in terms of the NIG parameters:

$$\bar{c} = \mathbb{E}[c] = \mathbb{E}[\mathbb{E}[c|\mu, \sigma^2]] = \mathbb{E}[\mu] = \gamma, \quad (15)$$

$$U = \text{Var}[c] = U^{\text{alea}} + U^{\text{epis}}, \quad (16)$$

$$U^{\text{alea}} = \mathbb{E}[\text{Var}[c|\mu, \sigma^2]] = \mathbb{E}[\sigma^2] = \frac{\beta}{\alpha - 1}, \quad (17)$$

$$U^{\text{epis}} = \text{Var}[\mathbb{E}[c|\mu, \sigma^2]] = \text{Var}[\mu] = \frac{\beta}{(\alpha - 1)\nu}. \quad (18)$$

Since the Evidential NeRF model directly predicts uncertainties and shape scores instead of NIG parameters, the NIG parameters can be reformulated as

$$\gamma = \bar{c}, \quad \nu = \frac{U^{\text{alea}}}{U^{\text{epis}}}, \quad (19)$$

$$\alpha = 1 + \sum_{i=1}^N \tilde{w}_i \tilde{\alpha}_i, \quad \beta = U^{\text{alea}}(\alpha - 1), \quad (20)$$

where \bar{c} , U^{alea} , and U^{epis} are obtained from the voxel-to-pixel propagation process in Equations (12) and (13), $\tilde{\alpha}_i$ is the voxel's shape score, and $\tilde{w}_i := w_i / \sum_{j=1}^N w_j$ is the normalized weight that determines how much a voxel's shape score contributes to the NIG shape parameter α of the pixel.

4.4. Learning

Based on Equations (4) and (14), a pixel color c marginally follows a Student's t distribution

$$c \sim t\left(\gamma, \frac{\beta(\nu + 1)}{\alpha\nu}, 2\alpha\right), \quad (21)$$

Dataset	Method	PSNR \uparrow	SSIM \uparrow	LPIPS \downarrow	NLL \downarrow	AUSE RMSE \downarrow	AUSE MAE \downarrow	AUCE \downarrow
LF [46]	Dropout [7]	28.0894	0.9065	0.0561	5.6139	0.0127	0.0049	0.2052
	Normal [17]	28.1477	0.9141	0.0514	-1.9191	0.0102	0.0048	0.1508
	MoL [35]	28.0407	0.9046	0.0769	-1.3919	0.0182	0.0061	0.3114
	BayesRays [10]	28.4782	0.9173	0.0482	0.6212	0.0369	0.0178	0.4759
	Ensembles [21]	29.3283	0.9307	0.0405	0.4942	0.0062	0.0024	0.1871
	DANE [40]	29.3283	0.9307	0.0405	-0.1474	0.0098	0.0039	0.1198
	Evidential	29.9318	0.9346	0.0354	-2.4828	0.0069	0.0026	0.1056
LLFF [23]	Dropout [7]	17.1558	0.4436	0.4465	92.1885	0.0741	0.0424	0.3951
	Normal [17]	16.5284	0.4106	0.4013	10.9719	0.0709	0.0445	0.2884
	MoL [35]	16.3826	0.4388	0.4536	3.6559	0.0842	0.0408	0.3075
	BayesRays [10]	17.5240	0.4719	0.4124	3.8344	0.0973	0.0620	0.4879
	Ensembles [21]	17.9220	0.5104	0.3942	10.5361	0.0508	0.0251	0.2880
	DANE [40]	17.9220	0.5104	0.3942	9.4168	0.0515	0.0258	0.2767
	Evidential	17.8754	0.5052	0.3776	2.2586	0.0595	0.0306	0.3710
RobustNeRF [32]	Dropout [7]	24.8334	0.8124	0.1728	22.5366	0.0281	0.0160	0.3055
	Normal [17]	25.4664	0.8465	0.1387	10.1970	0.0409	0.0272	0.2026
	MoL [35]	23.5230	0.7819	0.2155	-1.2758	0.0354	0.0204	0.1386
	BayesRays [10]	25.4561	0.8300	0.1559	0.2485	0.0411	0.0235	0.4423
	Ensembles [21]	26.2294	0.8580	0.1401	4.8797	0.0163	0.0098	0.2526
	DANE [40]	26.2294	0.8580	0.1401	4.1391	0.0277	0.0152	0.1917
	Evidential	25.8585	0.8585	0.1195	-1.3215	0.0265	0.0163	0.2024

Table 1. Quantitative results of scene reconstruction and uncertainty quantification on three datasets, averaged over three independent runs. Colored cells denote the **first**, **second**, and **third** best results. See per-scene statistics with standard deviations in supplementary Section 9.

where $t(\mu_t, \sigma_t^2, \nu_t)$ denotes a Student’s t distribution with location μ_t , scale σ_t , and degrees of freedom ν_t . The model is trained via maximum likelihood estimation by minimizing the negative log-likelihood (NLL) of the ground truth

$$\mathcal{L}_{\text{nll}} = -\log p(c^{\text{gt}}|\gamma, \nu, \alpha, \beta) \quad (22)$$

$$= \frac{1}{2} \log \frac{\pi}{\nu} - \alpha \log \Omega + \log \frac{\Gamma(\alpha)}{\Gamma(\alpha + \frac{1}{2})} + \left(\alpha + \frac{1}{2} \right) \log((c^{\text{gt}} - \gamma)^2 \nu + \Omega), \quad (23)$$

where $c^{\text{gt}} \in [0, 1]$ is the ground truth pixel color, $\Omega = 2\beta(\nu + 1)$, and Γ represents the Gamma function. See derivations in Section 8.

Different values of ν and β may result in the same scale of the t distribution so long as the ratio is $\beta(\nu+1)/\nu$ is fixed. To resolve this ambiguity and also to suppress excessive evidence assigned to inaccurate predictions, a regularizer [1] is introduced to the loss function as

$$\mathcal{L}_{\text{reg}} = |c^{\text{gt}} - \gamma|(2\nu + \alpha), \quad (24)$$

where $|c^{\text{gt}} - \gamma|$ is the absolute error of prediction and $2\nu + \alpha$ is the count of virtual observations representing the evidence [1]. Therefore, the total loss is written as

$$\mathcal{L} = \mathcal{L}_{\text{nll}} + \lambda_{\text{reg}} \mathcal{L}_{\text{reg}}, \quad (25)$$

where $\lambda_{\text{reg}} > 0$ is the regularization coefficient.

Lastly, we generalize our color channel assumption from a single channel to three for RGB color modeling. We assume that the three color channels have different means but the same uncertainty, due to the high correlation of variance in different color channels of the same pixel [22, 28]. Practically, the output dimension of color prediction head in Equation (9) is set to three, predicting the voxel’s mean RGB color as $\bar{c}_i \in [0, 1]^3$, and the uncertainty-related parameters are broadcast to all color channels during training.

5. Experiments

5.1. Settings

Datasets. We test the UQ methods on three 3D scene reconstruction datasets: Light Field (LF) [46], Local Light Field Fusion (LLFF) [23], and RobustNeRF [32]. For LF, we test on the four scenes following the setup in [10] with the same train–test split. For LLFF, we employ its eight scenes and adopt the train–test split of [27], training with only three input views to assess UQ performance under sparse-view conditions. For RobustNeRF, we evaluate on its four scenes following their protocol of training on cluttered images only and testing on clean ones.

Metrics. We evaluate the method performance based on the accuracy of both the rendered images and the uncertainty estimates. For images, we report PSNR, SSIM, and

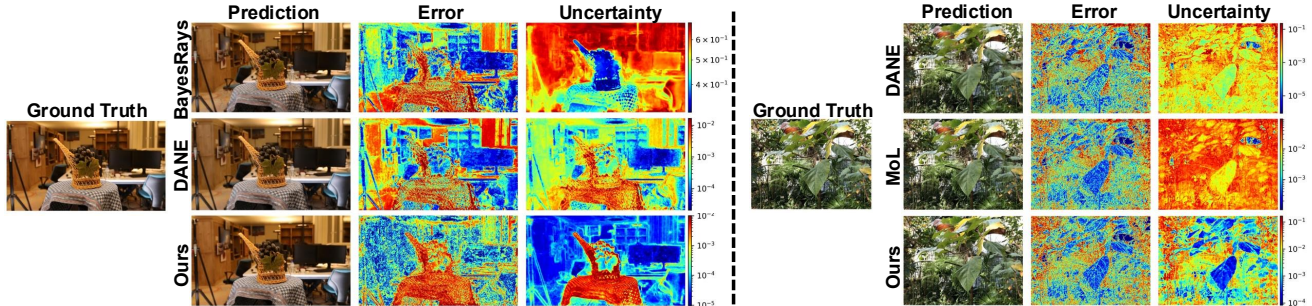


Figure 2. Qualitative comparison against previous methods on two example scenes, with image reconstructions, error maps, and uncertainty maps. Histogram equalization is conducted on the error maps to highlight the error regions. Our method’s uncertainty is total uncertainty. In general, our total uncertainty maps demonstrate superior alignment with predictive errors, confirming that the joint modeling of aleatoric and epistemic uncertainties yields the most faithful uncertainty estimates. More qualitative figures are provided in Section 10.

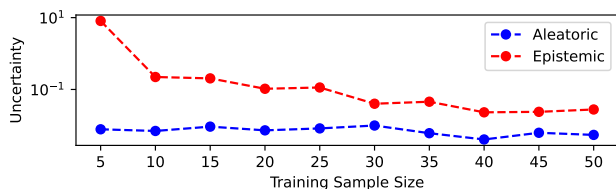


Figure 3. Test AU and EU vs. training sample size. AU remains stable while EU significantly declines with more data observed.

LPIPS to reflect the image reconstruction quality. For uncertainties, we use negative log-likelihood (NLL), area under sparsification error (AUSE) with respect to both RMSE and MAE, and area under calibration error (AUCE), measuring the quality of uncertainty estimates in terms of distributional fit, error ranking, and calibration accuracy.

Baselines. We select two methods from each of the three categories discussed in Section 2. For closed-form likelihood models, we use the normal distribution approach [17] adopted in [22] and [28] and mixture of Laplace distributions (MoL) employed in [35] and [34]. For Bayesian methods, we include the classical Monte Carlo dropout [7] and a more recent NeRF UQ method BayesRays [10]. For ensemble methods, we consider naive deep ensembles [21] and density-aware NeRF ensembles (DANE) [40].

Implementation. Prior benchmarks on NeRF uncertainty quantification suffer from varying choices of data splits, model architectures, and training schemes. To isolate UQ method effects from engineering confounds, we establish a new standardized benchmark to focus comparison on the underlying UQ approaches themselves. First, for data split, we follow the aforementioned scheme for all models. Second, for architecture, we use nerfacto model in [41] to implement all methods for efficiency. For likelihood models, the only difference is the output layer size and the loss function. For Bayesian methods, Monte Carlo dropout is implemented with a dropout probability 0.2, trained once and sampled five times at inference, while BayesRays follows their official implementation. For ensembles, both naive en-

Mode	Baseline	Dropout	Normal	MoL	Ens.	DANE	Ours
Train/min.↓	11.84	88.54	12.22	12.71	59.22	59.22	13.57
Infer/FPS↑	4.88	0.09	4.71	4.42	0.96	0.96	4.67

Table 2. Average training time per 30k steps and inference FPS of baseline nerfacto and different UQ methods on an A6000 GPU.

sembles and DANE are implemented by training five models independently. Third, in training, we adopt the default batch size, optimizer, and learning rate scheduler of nerfacto for all methods and train for 5k iterations for LLFF and 30k iterations for LF and RobustNeRF, chosen based on the convergence speed on each dataset. For stability, we run each method independently for three times and report the averaged metrics. The benchmark codebase will be released upon paper acceptance to ensure that all results can be faithfully reproduced by the community.

5.2. Results

Quantitative results. The quantitative performance of the uncertainty quantification methods is detailed in Table 1 with per-scene statistics provided in Section 9.

For **prediction accuracy**, as BayesRays estimates uncertainty in a post-hoc manner, it does not alter the image reconstruction metrics, which can be regarded as the baseline nerfacto accuracy. Compared to this baseline, likelihood and Bayesian methods (Dropout, Normal, MoL) generally struggle to preserve the image reconstruction accuracy, indicating that their predictive performance is compromised in exchange for uncertainty estimation. Ensemble-based methods provide faithful reconstructions, but they are extremely inefficient due to their substantial computational cost in both training and inference. In contrast, Evidential NeRF, while being efficient, consistently outperforms baseline in image reconstruction, demonstrating that our uncertainties need not come at the expense of rendering fidelity. Remarkably, with only a single network trained and a single forward pass required at inference, the evidential approach achieves prediction accuracy comparable to, and in 6 out of 9 image reconstruction metrics even surpassing, the compu-

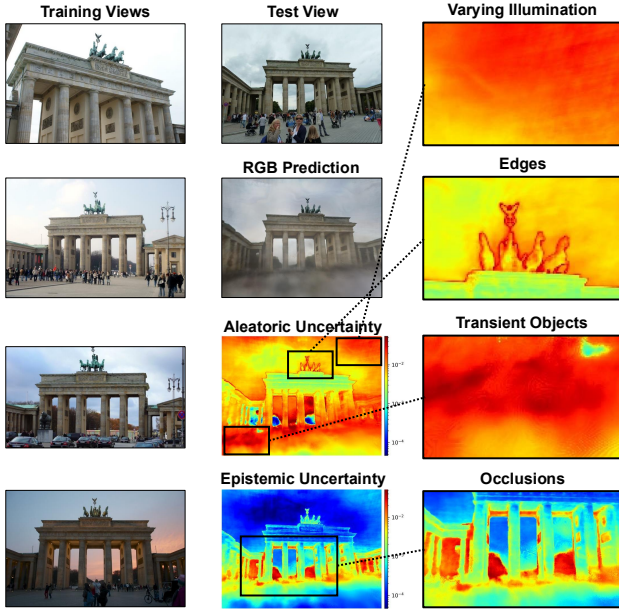


Figure 4. Aleatoric and epistemic uncertainties of a scene in the wild. AU arises from intrinsic data variability captured in the training set, including radiance variation (e.g., sky regions due to changing illumination), high-frequency regions (e.g., scene edges), and the presence of transient objects (e.g., pedestrians). EU indicates the model’s lack of knowledge, prominently appearing in occluded regions where training supervision is insufficient (e.g., the trees behind and thus occluded by the gate).

tationally expensive ensemble methods.

For **uncertainty quantification**, our method achieves the lowest NLL across all three datasets, demonstrating the best distributional fit. Compared to a normal distribution with fixed mean and variance, a normal distribution with random mean and variance increases test data likelihood by factors of 1.8, 6083.3, and 100559.0 on the three datasets, respectively. This tremendous improvement is because the fixed mean and variance assumption used by classical normal-based UQ only captures the aleatoric variations within the training data while overlooking epistemic uncertainty. The likelihood gain is less pronounced on LF because its test images are adjacent to the training views, thus the distribution shift is relatively insignificant. As for AUSE and AUCE, ensemble-based methods achieve the strongest results in general, which is expected given their ability to represent variability through multiple models. Nevertheless, our evidential approach remains highly competitive, often ranking second only to ensembles, demonstrating that jointly modeling aleatoric and epistemic factors yields uncertainty estimates with stronger correlation with errors and improved calibration.

Qualitative results. We qualitatively evaluate our Evidential NeRF against other uncertainty quantification methods in Figure 2 and Section 10. A primary goal of UQ is to

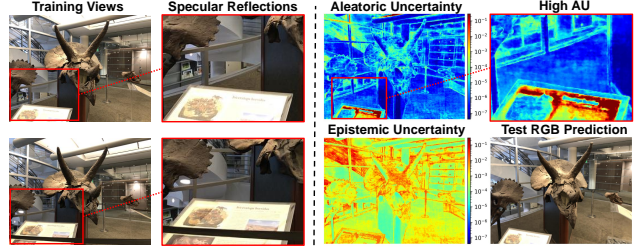


Figure 5. A case where AU dominates EU. The highly reflective surface of the display case in the foreground incurs specular reflections. AU arises due to the presence of data noise caused by the inconsistency of light across different training views.

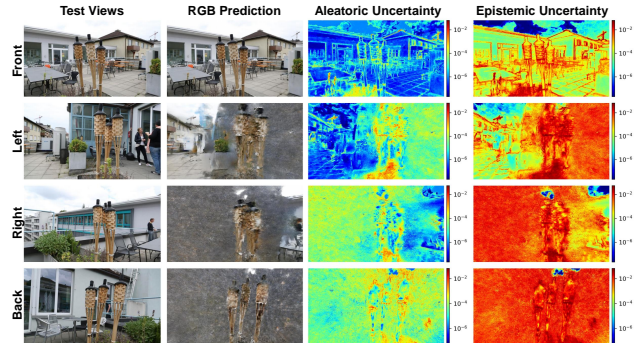


Figure 6. A case where EU dominates AU. The model is trained only by 5 images from the front and asked to render the scene from all the viewing angles. EU arises due to the lack of knowledge during training on the views out of training distribution.

produce uncertainty maps that accurately identify potential model failures. Previous methods, by neglecting either the aleatoric or epistemic component of predictive uncertainty, often fall short of accurately delimiting regions of predictive inaccuracy. In contrast, by considering both components, our method demonstrates superior alignment with the reconstruction error maps. This suggests that jointly modeling data noise and the model knowledge gap is essential for generating the most reliable uncertainty estimates.

Uncertainty scaling with data. We investigate the effect of training sample size on the magnitude of aleatoric and epistemic uncertainties in Figure 3. Focusing on this example LLFF scene, we reserve 10% of its views for testing and incrementally select 5 to 50 images from the remaining data for training. As the training sample size increases, the test AU remains relatively stable, while the EU exhibits a considerable decline. The result verifies the fundamental difference between the two types of uncertainty: AU is irreducible as intrinsic data noise, while EU is reducible by increasing the model’s exposure to more data.

Aleatoric and epistemic factors in 3D scenes. Several scenarios where aleatoric and epistemic uncertainties emerge are respectively presented in Figures 4 to 6. Figure 4 illustrates an in-the-wild scene with several aleatoric factors (varying illumination, high-frequency edge regions, tran-

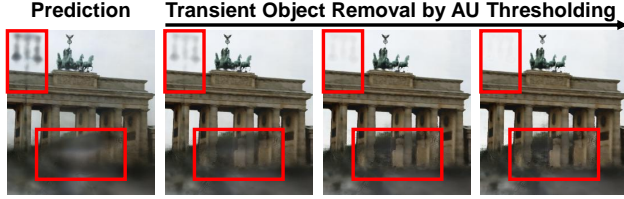


Figure 7. Scene cleaning based on aleatoric uncertainty as a post-processing step for floater removal. Voxels with AU above a certain threshold have their density reduced to become more transparent. By reducing the threshold, more artifacts can be eliminated.

sient objects) and an epistemic factor (partial occlusions). Figure 5 showcases a scenario with a reflective object, where aleatoric light variation is the dominant source of potential rendering error. Figure 6 demonstrates an out-of-distribution example where the model is asked to render the scene from angles that never appeared during training, showing that the lack of model knowledge about these unseen views is the primary cause of predictive failure.

Computational efficiency. We report the total training time and inference frames per second (FPS) of baseline nerfacto and different UQ methods in Table 2. Compared to other UQ methods, in training, our evidential approach is only slightly slower than other two likelihood models while being significantly faster than the ensemble methods. As for inference, since our approach directly predicts uncertainty fields, it is more efficient than the methods which require computing uncertainty from the predicted parameters, such as MoL. **Note:** As BayesRays learns a spatial uncertainty field through a dedicated post-hoc procedure after NeRF convergence rather than the typical volumetric rendering pipeline, it is excluded from this comparison. Since nerfacto runs on Tiny CUDA Neural Networks [25], which does not support dropout, dropout is implemented without acceleration, making it naturally slower than other methods.

5.3. Applications

We demonstrate two example applications using aleatoric and epistemic uncertainties respectively in Figures 7 and 8.

Scene cleaning. Training NeRFs on unconstrained images often leads to inaccurate predictions due to radiance inconsistencies from uncontrolled lighting changes or transient objects, which are irreducible data noise explained by aleatoric uncertainty. As a robust indicator of geometric artifacts, AU-based scene cleaning can be applied as a post-processing procedure to eliminate noise in the renderings. Figure 7 presents an example where the erroneous floaters of the rendering can be progressively removed by gradually changing the AU threshold to suppress voxel densities.

Active learning. As a proxy of lack of model knowledge, epistemic uncertainty is an ideal metric for active learning. Figure 8 illustrates a next-best-view planning experiment on an LLFF scene. Starting from an initial training set of 5 im-

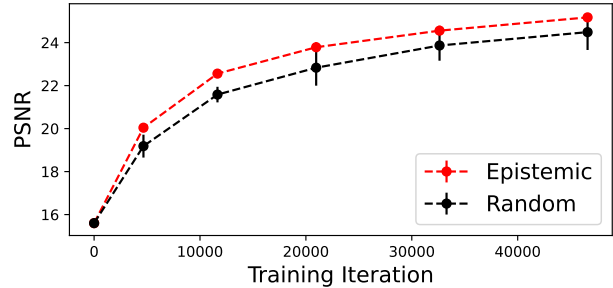


Figure 8. Mean and standard deviation of test PSNR of three runs on *Horns* scene, with two active sampling strategies: EU-based selection and random selection. The samples identified via epistemic uncertainty are more informative for model learning.

ages, an Evidential NeRF is trained iteratively by 5 rounds. In each round, the model is trained by 5 epochs with all the current training images and then tested on a holdout test set, before choosing 5 additional images from the remaining data to add to the training pool. Two sampling strategies for data selection are compared: choosing the images with the most EU and choosing images randomly. The average and standard deviation of three independent runs of each selection scheme are reported. Active selection based on EU gives noticeably higher PSNR than random selection, indicating the samples with higher epistemic uncertainty are more informative for model learning.

6. Conclusion

Despite the remarkable efficacy of neural radiance fields in photorealistic 3D scene reconstruction, the absence of robust predictive uncertainty quantification significantly hinders their deployment in safety-critical domains. While some uncertainty quantification methods have been proposed for NeRFs, none of them provides a mechanism for quantifying both aleatoric and epistemic components of the scene rendering uncertainty. Considering that 3D scene modeling is inherently subject to both data volatility and model ignorance, limiting uncertainty quantification to a single component is suboptimal.

In this paper, we introduce Evidential Neural Radiance Fields, a principled probabilistic framework that resolves this critical gap, representing a significant step toward explainable and reliable implicit 3D modeling. Our approach seamlessly adapts evidential deep learning to the hierarchical nature of NeRFs through a voxel-to-pixel aleatoric and epistemic uncertainty propagation paradigm. Through extensive experiments on three standardized benchmarks, Evidential NeRF demonstrates its superiority in both image reconstruction fidelity and uncertainty estimation quality compared to other methods, in the meantime, identifying the aleatoric and epistemic factors that contribute to predictive uncertainty within a variety of 3D scenes.

References

- [1] Alexander Amini, Wilko Schwarting, Ava Soleimany, and Daniela Rus. Deep evidential regression. *Advances in neural information processing systems*, 33:14927–14937, 2020. 1, 2, 5
- [2] Jonathan T Barron, Ben Mildenhall, Matthew Tancik, Peter Hedman, Ricardo Martin-Brualla, and Pratul P Srinivasan. Mip-nerf: A multiscale representation for anti-aliasing neural radiance fields. In *Proceedings of the IEEE/CVF international conference on computer vision*, pages 5855–5864, 2021. 2
- [3] Jonathan T Barron, Ben Mildenhall, Dor Verbin, Pratul P Srinivasan, and Peter Hedman. Mip-nerf 360: Unbounded anti-aliased neural radiance fields. In *Proceedings of the IEEE/CVF conference on computer vision and pattern recognition*, pages 5470–5479, 2022.
- [4] Jonathan T Barron, Ben Mildenhall, Dor Verbin, Pratul P Srinivasan, and Peter Hedman. Zip-nerf: Anti-aliased grid-based neural radiance fields. In *Proceedings of the IEEE/CVF International Conference on Computer Vision*, pages 19697–19705, 2023.
- [5] Anpei Chen, Zexiang Xu, Andreas Geiger, Jingyi Yu, and Hao Su. Tensorf: Tensorial radiance fields. In *European conference on computer vision*, pages 333–350. Springer, 2022.
- [6] Zhiqin Chen, Thomas Funkhouser, Peter Hedman, and Andrea Tagliasacchi. Mobilenerf: Exploiting the polygon rasterization pipeline for efficient neural field rendering on mobile architectures. In *Proceedings of the IEEE/CVF Conference on Computer Vision and Pattern Recognition*, pages 16569–16578, 2023. 2
- [7] Yarin Gal and Zoubin Ghahramani. Dropout as a bayesian approximation: Representing model uncertainty in deep learning. In *international conference on machine learning*, pages 1050–1059. PMLR, 2016. 1, 2, 5, 6
- [8] Stephan J Garbin, Marek Kowalski, Matthew Johnson, Jamie Shotton, and Julien Valentin. Fastnerf: High-fidelity neural rendering at 200fps. In *Proceedings of the IEEE/CVF international conference on computer vision*, pages 14346–14355, 2021. 2
- [9] Jakob Gawlikowski, Cedric Rovile Njéutcheu Tassi, Mohsin Ali, Jongseok Lee, Matthias Humt, Jianxiang Feng, Anna Kruspe, Rudolph Triebel, Peter Jung, Ribana Roscher, et al. A survey of uncertainty in deep neural networks. *Artificial Intelligence Review*, 56(Suppl 1):1513–1589, 2023. 1
- [10] Lily Goli, Cody Reading, Silvia Sellán, Alec Jacobson, and Andrea Tagliasacchi. Bayes’ rays: Uncertainty quantification for neural radiance fields. In *Proceedings of the IEEE/CVF Conference on Computer Vision and Pattern Recognition*, pages 20061–20070, 2024. 2, 5, 6
- [11] Lei He, Leheng Li, Wenchao Sun, Zeyu Han, Yichen Liu, Sifa Zheng, Jianqiang Wang, and Keqiang Li. Neural radiance field in autonomous driving: A survey. *arXiv preprint arXiv:2404.13816*, 2024. 1
- [12] Wenchong He, Zhe Jiang, Tingsong Xiao, Zelin Xu, and Yukun Li. A survey on uncertainty quantification methods for deep learning, 2024. 1
- [13] Tao Hu, Shu Liu, Yilun Chen, Tiancheng Shen, and Jiaya Jia. Efficientnerf efficient neural radiance fields. In *Proceedings of the IEEE/CVF Conference on Computer Vision and Pattern Recognition*, pages 12902–12911, 2022. 2
- [14] Eyke Hüllermeier and Willem Waegeman. Aleatoric and epistemic uncertainty in machine learning: An introduction to concepts and methods. *Machine learning*, 110(3):457–506, 2021. 1
- [15] Ajay Jain, Matthew Tancik, and Pieter Abbeel. Putting nerf on a diet: Semantically consistent few-shot view synthesis. In *Proceedings of the IEEE/CVF International Conference on Computer Vision*, pages 5885–5894, 2021. 2
- [16] Audun Jsang. *Subjective Logic: A formalism for reasoning under uncertainty*. Springer Publishing Company, Incorporated, 2018. 2
- [17] Alex Kendall and Yarin Gal. What uncertainties do we need in bayesian deep learning for computer vision? *Advances in neural information processing systems*, 30, 2017. 1, 2, 5, 6
- [18] Bernhard Kerbl, Georgios Kopanas, Thomas Leimkühler, and George Drettakis. 3d gaussian splatting for real-time radiance field rendering. *ACM Trans. Graph.*, 42(4):139–1, 2023. 1
- [19] Diederik P Kingma. Auto-encoding variational bayes. *arXiv preprint arXiv:1312.6114*, 2013. 2
- [20] Jonas Kulhanek, Songyou Peng, Zuzana Kukelova, Marc Pollefeys, and Torsten Sattler. Wildgaussians: 3d gaussian splatting in the wild. *arXiv preprint arXiv:2407.08447*, 2024. 1
- [21] Balaji Lakshminarayanan, Alexander Pritzel, and Charles Blundell. Simple and scalable predictive uncertainty estimation using deep ensembles. *Advances in neural information processing systems*, 30, 2017. 1, 2, 5, 6
- [22] Ricardo Martin-Brualla, Noha Radwan, Mehdi SM Sajjadi, Jonathan T Barron, Alexey Dosovitskiy, and Daniel Duckworth. Nerf in the wild: Neural radiance fields for unconstrained photo collections. In *Proceedings of the IEEE/CVF conference on computer vision and pattern recognition*, pages 7210–7219, 2021. 1, 2, 3, 5, 6
- [23] Ben Mildenhall, Pratul P Srinivasan, Rodrigo Ortiz-Cayon, Nima Khademi Kalantari, Ravi Ramamoorthi, Ren Ng, and Abhishek Kar. Local light field fusion: Practical view synthesis with prescriptive sampling guidelines. *ACM Transactions on Graphics (TOG)*, 38(4):1–14, 2019. 5
- [24] Ben Mildenhall, Pratul P. Srinivasan, Matthew Tancik, Jonathan T. Barron, Ravi Ramamoorthi, and Ren Ng. Nerf: Representing scenes as neural radiance fields for view synthesis. In *ECCV*, 2020. 1, 2
- [25] Thomas Müller. tiny-cuda-nn, 2021. 8
- [26] Thomas Müller, Alex Evans, Christoph Schied, and Alexander Keller. Instant neural graphics primitives with a multiresolution hash encoding. *ACM transactions on graphics (TOG)*, 41(4):1–15, 2022. 2
- [27] Michael Niemeyer, Jonathan T Barron, Ben Mildenhall, Mehdi SM Sajjadi, Andreas Geiger, and Noha Radwan. Regnerf: Regularizing neural radiance fields for view synthesis from sparse inputs. In *Proceedings of the IEEE/CVF Conference on Computer Vision and Pattern Recognition*, pages 5480–5490, 2022. 2, 5

- [28] Xuran Pan, Zihang Lai, Shiji Song, and Gao Huang. Activenerf: Learning where to see with uncertainty estimation. In *European Conference on Computer Vision*, pages 230–246. Springer, 2022. 1, 2, 3, 5, 6
- [29] Weining Ren, Zihan Zhu, Boyang Sun, Jiaqi Chen, Marc Pollefeys, and Songyou Peng. Nerf on-the-go: Exploiting uncertainty for distractor-free nerfs in the wild. In *Proceedings of the IEEE/CVF Conference on Computer Vision and Pattern Recognition*, pages 8931–8940, 2024. 1
- [30] Danilo Rezende and Shakir Mohamed. Variational inference with normalizing flows. In *International conference on machine learning*, pages 1530–1538. PMLR, 2015. 2
- [31] Hippolyt Ritter, Aleksandar Botev, and David Barber. A scalable laplace approximation for neural networks. In *6th international conference on learning representations, ICLR 2018-conference track proceedings*. International Conference on Representation Learning, 2018. 2
- [32] Sara Sabour, Suhani Vora, Daniel Duckworth, Ivan Krasin, David J Fleet, and Andrea Tagliasacchi. Robustnerf: Ignoring distractors with robust losses. In *Proceedings of the IEEE/CVF conference on computer vision and pattern recognition*, pages 20626–20636, 2023. 5
- [33] Murat Sensoy, Lance Kaplan, and Melih Kandemir. Evidential deep learning to quantify classification uncertainty. *Advances in neural information processing systems*, 31, 2018. 1, 2
- [34] Seunghyeon Seo, Yeonjin Chang, and Nojun Kwak. Flipnerf: Flipped reflection rays for few-shot novel view synthesis. In *Proceedings of the IEEE/CVF International Conference on Computer Vision*, pages 22883–22893, 2023. 1, 2, 6
- [35] Seunghyeon Seo, Donghoon Han, Yeonjin Chang, and Nojun Kwak. Mixnerf: Modeling a ray with mixture density for novel view synthesis from sparse inputs. In *Proceedings of the IEEE/CVF Conference on Computer Vision and Pattern Recognition*, pages 20659–20668, 2023. 1, 2, 5, 6
- [36] Jianxiong Shen, Adria Ruiz, Antonio Agudo, and Francesc Moreno-Noguer. Stochastic neural radiance fields: Quantifying uncertainty in implicit 3d representations. In *2021 International Conference on 3D Vision (3DV)*, pages 972–981. IEEE, 2021. 1, 2
- [37] Jianxiong Shen, Antonio Agudo, Francesc Moreno-Noguer, and Adria Ruiz. Conditional-flow nerf: Accurate 3d modelling with reliable uncertainty quantification. In *European Conference on Computer Vision*, pages 540–557. Springer, 2022. 1, 2
- [38] Jianxiong Shen, Ruijie Ren, Adria Ruiz, and Francesc Moreno-Noguer. Estimating 3d uncertainty field: Quantifying uncertainty for neural radiance fields. In *2024 IEEE International Conference on Robotics and Automation (ICRA)*, pages 2375–2381. IEEE, 2024. 1
- [39] Cheng Sun, Min Sun, and Hwann-Tzong Chen. Direct voxel grid optimization: Super-fast convergence for radiance fields reconstruction. In *Proceedings of the IEEE/CVF conference on computer vision and pattern recognition*, pages 5459–5469, 2022. 1
- [40] Niko Sündnerhauf, Jad Abou-Chakra, and Dimity Miller. Density-aware nerf ensembles: Quantifying predictive uncertainty in neural radiance fields. In *2023 IEEE International Conference on Robotics and Automation (ICRA)*, pages 9370–9376. IEEE, 2023. 1, 2, 5, 6
- [41] Matthew Tancik, Ethan Weber, Evonne Ng, Ruilong Li, Brent Yi, Justin Kerr, Terrance Wang, Alexander Kristoffersen, Jake Austin, Kamyar Salahi, Abhik Ahuja, David McAllister, and Angjoo Kanazawa. Nerfstudio: A modular framework for neural radiance field development. In *ACM SIGGRAPH 2023 Conference Proceedings*, 2023. 6
- [42] Dor Verbin, Peter Hedman, Ben Mildenhall, Todd Zickler, Jonathan T Barron, and Pratul P Srinivasan. Ref-nerf: Structured view-dependent appearance for neural radiance fields. In *2022 IEEE/CVF Conference on Computer Vision and Pattern Recognition (CVPR)*, pages 5481–5490. IEEE, 2022. 2
- [43] Guangming Wang, Lei Pan, Songyou Peng, Shaohui Liu, Chenfeng Xu, Yanzi Miao, Wei Zhan, Masayoshi Tomizuka, Marc Pollefeys, and Hesheng Wang. Nerf in robotics: A survey. *arXiv preprint arXiv:2405.01333*, 2024. 1
- [44] Xin Wang, Shu Hu, Heng Fan, Hongtu Zhu, and Xin Li. Neural radiance fields in medical imaging: Challenges and next steps. *arXiv preprint arXiv:2402.17797*, 2024. 1
- [45] Qiangeng Xu, Zexiang Xu, Julien Philip, Sai Bi, Zhixin Shu, Kalyan Sunkavalli, and Ulrich Neumann. Pointnerf: Point-based neural radiance fields. In *Proceedings of the IEEE/CVF conference on computer vision and pattern recognition*, pages 5438–5448, 2022. 2
- [46] Kaan Yücer, Alexander Sorkine-Hornung, Oliver Wang, and Olga Sorkine-Hornung. Efficient 3d object segmentation from densely sampled light fields with applications to 3d reconstruction. *ACM Transactions on Graphics (TOG)*, 35(3): 1–15, 2016. 5

Evidential Neural Radiance Fields

Supplementary Material

7. Derivations: Voxel-to-Pixel Propagation of Radiance and Uncertainty

This section derives the propagation formulae of radiance and uncertainties specified in Equations (12) and (13).

The mean color aggregation formula follows directly from the linearity of expectation, which does not require any independence assumption.

$$\bar{c} = \mathbb{E}[c] = \mathbb{E} \left[\sum_{i=1}^N w_i c_i \right] = \sum_{i=1}^N w_i \mathbb{E}[c_i] = \sum_{i=1}^N w_i \bar{c}_i. \quad (26)$$

Deriving the three uncertainty propagation formulae each requires its own independence assumption. However, only two, and any two, of these three assumptions are necessary to derive all the three formulae.

Assumption 1. *The voxel colors are independent, i.e., $c_i \perp\!\!\!\perp c_j, \forall i \neq j$.*

Assumption 2. *The voxel colors are conditionally independent given the conditional means and variances, i.e., $c_i \perp\!\!\!\perp c_j \mid \theta, \forall i \neq j$.*

Assumption 3. *The voxel colors' conditional means are independent, i.e., $\mu_i \perp\!\!\!\perp \mu_j, \forall i \neq j$.*

With these assumptions, it can be shown that

$$U = \text{Var}[c] = \text{Var} \left[\sum_{i=1}^N w_i c_i \right] \stackrel{\text{A.1}}{=} \sum_{i=1}^N w_i^2 \text{Var}[c_i] = \sum_{i=1}^N w_i^2 U_i, \quad (27)$$

$$\begin{aligned} U^{\text{alea}} &= \mathbb{E}[\text{Var}[c \mid \theta]] = \mathbb{E} \left[\text{Var} \left[\sum_{i=1}^N w_i c_i \mid \theta \right] \right] \stackrel{\text{A.2}}{=} \mathbb{E} \left[\sum_{i=1}^N w_i^2 \text{Var}[c_i \mid \theta] \right] \\ &= \sum_{i=1}^N w_i^2 \mathbb{E}[\text{Var}[c_i \mid \theta]] = \sum_{i=1}^N w_i^2 \mathbb{E}[\text{Var}[c_i \mid \mu_i, \sigma_i^2]] = \sum_{i=1}^N w_i^2 U_i^{\text{alea}}, \end{aligned} \quad (28)$$

$$\begin{aligned} U^{\text{epis}} &= \text{Var}[\mathbb{E}[c \mid \theta]] = \text{Var} \left[\mathbb{E} \left[\sum_{i=1}^N w_i c_i \mid \theta \right] \right] = \text{Var} \left[\sum_{i=1}^N w_i \mathbb{E}[c_i \mid \theta] \right] \\ &\stackrel{\text{A.3}}{=} \sum_{i=1}^N w_i^2 \text{Var}[\mathbb{E}[c_i \mid \theta]] = \sum_{i=1}^N w_i^2 \text{Var}[\mathbb{E}[c_i \mid \mu_i, \sigma_i^2]] = \sum_{i=1}^N w_i^2 U_i^{\text{epis}}, \end{aligned} \quad (29)$$

where $\stackrel{\text{A.}n}{=}$ denotes the step where Assumption n is used.

These three equations are connected by the law of total variance, as

$$\underbrace{\text{Var}[c]}_U = \underbrace{\mathbb{E}[\text{Var}[c \mid \theta]]}_{U^{\text{alea}}} + \underbrace{\text{Var}[\mathbb{E}[c \mid \theta]]}_{U^{\text{epis}}}, \quad (30)$$

$$\underbrace{\text{Var}[c_i]}_{U_i} = \underbrace{\mathbb{E}[\text{Var}[c_i \mid \mu_i, \sigma_i^2]]}_{U_i^{\text{alea}}} + \underbrace{\text{Var}[\mathbb{E}[c_i \mid \mu_i, \sigma_i^2]]}_{U_i^{\text{epis}}}. \quad (31)$$

Therefore, any two of Equations (27) to (29) imply the third, and thus only two of Assumptions 1 to 3 are necessary to derive all the three equations.

8. Derivations: Pixel Radiance Marginal Distribution and Loss Function

This section derives the marginal distribution of pixel radiance and the negative log-likelihood loss in Equations (21) and (23).

Evidential NeRF defines each pixel radiance c by a hierarchical probabilistic model

$$c \mid \mu, \sigma^2 \sim \mathcal{N}(\mu, \sigma^2), \quad \mu \mid \sigma^2 \sim \mathcal{N}(\gamma, \sigma^2/\nu), \quad \sigma^2 \sim \Gamma^{-1}(\alpha, \beta), \quad (32)$$

where $\mathcal{N}(\cdot, \cdot)$ and $\Gamma^{-1}(\cdot, \cdot)$ respectively denote normal distribution and inverse-gamma distribution and $\gamma \in \mathbb{R}$, $\nu > 0$, $\alpha > 1$, and $\beta > 0$ are the evidential NIG parameters. Based on these prerequisites, we derive the marginal distribution and negative log-likelihood of the pixel color c .

The probability density functions of the distributions in Equation (32) are respectively given by

$$p(c \mid \mu, \sigma^2) = \frac{1}{\sqrt{2\pi\sigma^2}} \exp\left(-\frac{(c-\mu)^2}{2\sigma^2}\right), \quad (33)$$

$$p(\mu \mid \sigma^2) = \frac{\sqrt{\nu}}{\sqrt{2\pi\sigma^2}} \exp\left(-\frac{(\mu-\gamma)^2\nu}{2\sigma^2}\right), \quad (34)$$

$$p(\sigma^2) = \frac{\beta^\alpha}{\Gamma(\alpha)} (\sigma^2)^{-\alpha-1} \exp\left(-\frac{\beta}{\sigma^2}\right). \quad (35)$$

It can therefore be shown that

$$p(c \mid \sigma^2) \quad (36)$$

$$= \int_{-\infty}^{\infty} p(c \mid \mu, \sigma^2) p(\mu \mid \sigma^2) d\mu \quad (37)$$

$$= \int_{-\infty}^{\infty} \frac{1}{\sqrt{2\pi\sigma^2}} \exp\left(-\frac{(c-\mu)^2}{2\sigma^2}\right) \frac{\sqrt{\nu}}{\sqrt{2\pi\sigma^2}} \exp\left(-\frac{(\mu-\gamma)^2\nu}{2\sigma^2}\right) d\mu \quad (38)$$

$$= \int_{-\infty}^{\infty} \frac{\sqrt{\nu}}{2\pi\sigma^2} \exp\left(-\frac{(c-\mu)^2 + (\mu-\gamma)^2\nu}{2\sigma^2}\right) d\mu \quad (39)$$

$$= \int_{-\infty}^{\infty} \frac{\sqrt{\nu}}{2\pi\sigma^2} \exp\left(-\frac{(\nu+1)\mu^2 - 2(c+\gamma\nu)\mu + (c^2 + \gamma^2\nu)}{2\sigma^2}\right) d\mu \quad (40)$$

$$= \frac{\sqrt{\nu}}{2\pi\sigma^2} \exp\left(-\frac{c^2 + \gamma^2\nu}{2\sigma^2}\right) \int_{-\infty}^{\infty} \exp\left(-\frac{(\nu+1)\mu^2 - 2(c+\gamma\nu)\mu}{2\sigma^2}\right) d\mu \quad (41)$$

$$= \frac{\sqrt{\nu}}{2\pi\sigma^2} \exp\left(-\frac{c^2 + \gamma^2\nu}{2\sigma^2}\right) \int_{-\infty}^{\infty} \exp\left(-\frac{(\mu - \frac{c+\gamma\nu}{\nu+1})^2 - (\frac{c+\gamma\nu}{\nu+1})^2}{\frac{2\sigma^2}{\nu+1}}\right) d\mu \quad (42)$$

$$= \frac{\sqrt{\nu}}{2\pi\sigma^2} \exp\left(-\frac{c^2 + \gamma^2\nu}{2\sigma^2}\right) \exp\left(\frac{(c+\gamma\nu)^2}{2\sigma^2(\nu+1)}\right) \int_{-\infty}^{\infty} \exp\left(-\frac{(\mu - \frac{c+\gamma\nu}{\nu+1})^2}{\frac{2\sigma^2}{\nu+1}}\right) d\mu \quad (43)$$

$$= \frac{\sqrt{\nu}}{2\pi\sigma^2} \exp\left(-\frac{c^2 + \gamma^2\nu}{2\sigma^2} + \frac{(c+\gamma\nu)^2}{2\sigma^2(\nu+1)}\right) \int_{-\infty}^{\infty} \sqrt{2\pi\frac{\sigma^2}{\nu+1}} \mathcal{N}\left(\mu; \frac{c+\gamma\nu}{\nu+1}, \frac{\sigma^2}{\nu+1}\right) d\mu \quad (44)$$

$$= \frac{\sqrt{\nu}}{2\pi\sigma^2} \sqrt{2\pi\frac{\sigma^2}{\nu+1}} \exp\left(-\frac{(c^2 + \gamma^2\nu)(\nu+1) - (c+\gamma\nu)^2}{2\sigma^2(\nu+1)}\right) \int_{-\infty}^{\infty} \mathcal{N}\left(\mu; \frac{c+\gamma\nu}{\nu+1}, \frac{\sigma^2}{\nu+1}\right) d\mu \quad (45)$$

$$= \frac{\sqrt{\nu}}{2\pi\sigma^2} \sqrt{2\pi\frac{\sigma^2}{\nu+1}} \exp\left(-\frac{(c^2 + \gamma^2\nu)(\nu+1) - (c+\gamma\nu)^2}{2\sigma^2(\nu+1)}\right) \quad (46)$$

$$= \sqrt{\frac{\nu}{2\pi\sigma^2(\nu+1)}} \exp\left(-\frac{(c-\gamma)^2\nu}{2\sigma^2(\nu+1)}\right), \quad (47)$$

i.e.,

$$c \mid \sigma^2 \sim \mathcal{N}\left(\gamma, \frac{\sigma^2(\nu+1)}{\nu}\right), \quad (48)$$

and thus,

$$p(c) \tag{49}$$

$$= \int_0^\infty p(c | \sigma^2) p(\sigma^2) d\sigma^2 \tag{50}$$

$$= \int_0^\infty \sqrt{\frac{\nu}{2\pi\sigma^2(\nu+1)}} \exp\left(-\frac{(c-\gamma)^2\nu}{2\sigma^2(\nu+1)}\right) \frac{\beta^\alpha}{\Gamma(\alpha)} (\sigma^2)^{-\alpha-1} \exp\left(-\frac{\beta}{\sigma^2}\right) d\sigma^2 \tag{51}$$

$$= \sqrt{\frac{\nu}{2\pi(\nu+1)}} \frac{\beta^\alpha}{\Gamma(\alpha)} \int_0^\infty \exp\left(-\frac{(c-\gamma)^2\nu}{2\sigma^2(\nu+1)} - \frac{\beta}{\sigma^2}\right) (\sigma^2)^{-\alpha-\frac{3}{2}} d\sigma^2 \tag{52}$$

$$= \sqrt{\frac{\nu}{2\pi(\nu+1)}} \frac{\beta^\alpha}{\Gamma(\alpha)} \int_0^\infty \exp\left(-\frac{\left(\frac{(c-\gamma)^2\nu}{2(\nu+1)} + \beta\right)}{\sigma^2}\right) (\sigma^2)^{-\alpha-\frac{3}{2}} d\sigma^2 \tag{53}$$

$$= \sqrt{\frac{\nu}{2\pi(\nu+1)}} \frac{\beta^\alpha}{\Gamma(\alpha)} \int_0^\infty \frac{\Gamma\left(\alpha + \frac{1}{2}\right)}{\left(\frac{(c-\gamma)^2\nu}{2(\nu+1)} + \beta\right)^{\alpha+\frac{1}{2}}} \Gamma^{-1}\left(\sigma^2; \alpha + \frac{1}{2}, \frac{(c-\gamma)^2\nu}{2(\nu+1)} + \beta\right) d\sigma^2 \tag{54}$$

$$= \sqrt{\frac{\nu}{2\pi(\nu+1)}} \frac{\beta^\alpha}{\Gamma(\alpha)} \frac{\Gamma\left(\alpha + \frac{1}{2}\right)}{\left(\frac{(c-\gamma)^2\nu}{2(\nu+1)} + \beta\right)^{\alpha+\frac{1}{2}}} \int_0^\infty \Gamma^{-1}\left(\sigma^2; \alpha + \frac{1}{2}, \frac{(c-\gamma)^2\nu}{2(\nu+1)} + \beta\right) d\sigma^2 \tag{55}$$

$$= \sqrt{\frac{\nu}{2\pi(\nu+1)}} \frac{\beta^\alpha}{\Gamma(\alpha)} \frac{\Gamma\left(\alpha + \frac{1}{2}\right)}{\left(\frac{(c-\gamma)^2\nu}{2(\nu+1)} + \beta\right)^{\alpha+\frac{1}{2}}} \tag{56}$$

$$= \frac{\Gamma\left(\alpha + \frac{1}{2}\right)}{\Gamma(\alpha) \sqrt{2\pi \frac{\beta(\nu+1)}{\nu}}} \left(\frac{(c-\gamma)^2}{2 \frac{\beta(\nu+1)}{\nu}} + 1\right)^{-(\alpha+\frac{1}{2})} \tag{57}$$

$$= \frac{\Gamma\left(\frac{\nu_t+1}{2}\right)}{\Gamma\left(\frac{\nu_t}{2}\right) \sqrt{\pi \nu_t \sigma_t^2}} \left(\frac{(c-\mu_t)^2}{\nu_t \sigma_t^2} + 1\right)^{-\frac{\nu_t+1}{2}}, \tag{58}$$

i.e.,

$$c \sim t\left(\mu_t = \gamma, \sigma_t^2 = \frac{\beta(\nu+1)}{\alpha\nu}, \nu_t = 2\alpha\right), \tag{59}$$

where $t(\mu_t, \sigma_t^2, \nu_t)$ denotes a Student's t distribution with location μ_t , scale σ_t , and degrees of freedom ν_t , and $\mathcal{N}(x; \cdot, \cdot)$ and $\Gamma^{-1}(x; \cdot, \cdot)$ represent their probability distribution densities at x . This yields Equation (21).

The negative log-likelihood of c can thereby be derived as

$$-\log p(c) \tag{60}$$

$$= -\log\left(\frac{\Gamma\left(\alpha + \frac{1}{2}\right)}{\Gamma(\alpha) \sqrt{2\pi \frac{\beta(\nu+1)}{\nu}}} \left(\frac{(c-\gamma)^2}{2 \frac{\beta(\nu+1)}{\nu}} + 1\right)^{-(\alpha+\frac{1}{2})}\right) \tag{61}$$

$$= \frac{1}{2} \log\left(2\pi \frac{\beta(\nu+1)}{\nu}\right) + \log \frac{\Gamma(\alpha)}{\Gamma\left(\alpha + \frac{1}{2}\right)} + \left(\alpha + \frac{1}{2}\right) \log\left(\frac{(c-\gamma)^2}{2 \frac{\beta(\nu+1)}{\nu}} + 1\right) \tag{62}$$

$$= \frac{1}{2} \log \frac{\pi}{\nu} + \frac{1}{2} \log(2\beta(\nu+1)) + \log \frac{\Gamma(\alpha)}{\Gamma\left(\alpha + \frac{1}{2}\right)} + \left(\alpha + \frac{1}{2}\right) \log\left(\frac{(c-\gamma)^2\nu}{2\beta(\nu+1)} + 1\right) \tag{63}$$

$$= \frac{1}{2} \log \frac{\pi}{\nu} - \alpha \log(2\beta(\nu+1)) + \log \frac{\Gamma(\alpha)}{\Gamma\left(\alpha + \frac{1}{2}\right)} + \left(\alpha + \frac{1}{2}\right) \log((c-\gamma)^2\nu + 2\beta(\nu+1)) \tag{64}$$

$$= \frac{1}{2} \log \frac{\pi}{\nu} - \alpha \log \Omega + \log \frac{\Gamma(\alpha)}{\Gamma\left(\alpha + \frac{1}{2}\right)} + \left(\alpha + \frac{1}{2}\right) \log((c-\gamma)^2\nu + \Omega), \tag{65}$$

where $\Omega = 2\beta(1 + \nu)$. This yields Equation (23).

9. Further Quantitative Results

In the main paper, quantitative results averaged across all scenes within each dataset are reported. Here, we provide the per-scene metrics in Tables 4 to 7, including the mean and standard deviation over three independent runs.

10. Further Qualitative Results

We present the qualitative comparison of the uncertainty methods on LF, LLFF, and RobustNeRF datasets in Figures 11 to 13, respectively. In addition, we also show the aleatoric and epistemic uncertainty maps of more scenes in the wild from Phototoursim dataset in Figure 14.

11. Further Discussions

Hyperparameter selection. The only hyperparameter of Evidential NeRF is the regularization coefficient in the loss function, which we select based on the quantitative metrics. Figure 9 illustrates how different regularization coefficients affect image reconstruction and uncertainty estimation. In general, both excessively small or large regularization coefficients lead to suboptimal performance, and the best hyperparameter value is inherently scene-dependent. The specific regularization coefficients utilized to produce the reported results are detailed in Table 3.

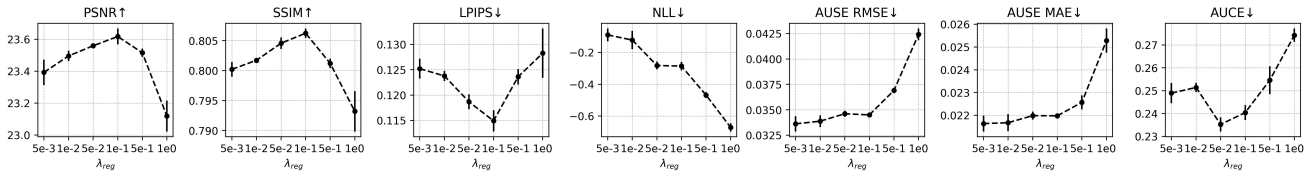


Figure 9. Sensitivity study of regularization coefficient’s effect on all the quantitative metrics of *Android* scene.

Scene	Africa	Basket	Statue	Torch	Fern	Flower	Fortress	Horns	Leaves	Orchids	Room	T-Rex	Android	Crab	Statue	Yoda
λ_{reg}	1e-1	1e-1	1e-3	1e-5	1e1	1e1	1e0	1e0	1e-4	1e0	1e0	1e-1	1e-1	5e-1	1e0	1e0

Table 3. The regularization coefficients used in each scene of LF, LLFF, and RobustNeRF datasets.

Mutual causes of aleatoric and epistemic uncertainties. Various complex elements in a 3D scene can lead to elevated levels of either aleatoric or epistemic uncertainty. However, attributing each specific factor exclusively to one type of uncertainty is often inappropriate, as many factors affect both uncertainties in different ways and to varying degrees. For example, transient objects increase AU due to color variations introduced by motion, while simultaneously raising EU through partial occlusions. Similarly, edges or high-frequency non-smooth regions tend to exhibit higher AU since their radiance is highly sensitive to input rays, as small inaccuracies in sensing, digitization, or poses can yield large radiance variations, resulting in nearly irreducible data uncertainty; meanwhile, the irregular geometry of such regions obstructs ray coverage and limits supervision signals from those surfaces, thereby increasing EU as well.

Uncertainties of transients. Transient objects in the scene can lead to both higher aleatoric and epistemic uncertainties. In practice, the uncertainties on the transient regions depend on the densities assigned to them by the model. Figure 10 showcases ten images from two RobustNeRF scenes where the model is trained by images with cluttered objects. It can be observed that the aleatoric and epistemic uncertainties on transients depend on their densities:

- If the model cannot disambiguate the transients and the floaters appear in the test renderings, both AU and EU are higher on them. This provides evidence that the model simultaneously receives inconsistent radiance signals (high AU) and lacks sufficient knowledge to determine the presence or geometry of transient objects (high EU).
- If the model resolves the transient objects (by minimizing their densities and removing them from volumetric rendering), the floaters disappear in the test image reconstructions and only AU remains high. This verifies that the model no longer lacks the knowledge to determine the presence of the transients but still records the color inconsistency from the training signals as high AU.

Limitation. NeRF models have two distinct outputs: density and radiance. The proposed Evidential NeRF framework, similar to other closed-form likelihood models, quantifies uncertainty in the predicted radiance c_i but treats the volumetric density ρ_i as deterministic, thus the randomness of density is not captured. This is a deliberate design choice which is fundamental to our method’s primary advantage of tractable and single-pass uncertainty propagation. This assumption enables the pixel-level aleatoric and epistemic uncertainties to be computed as a simple, closed-form weighted sum of their voxel-level

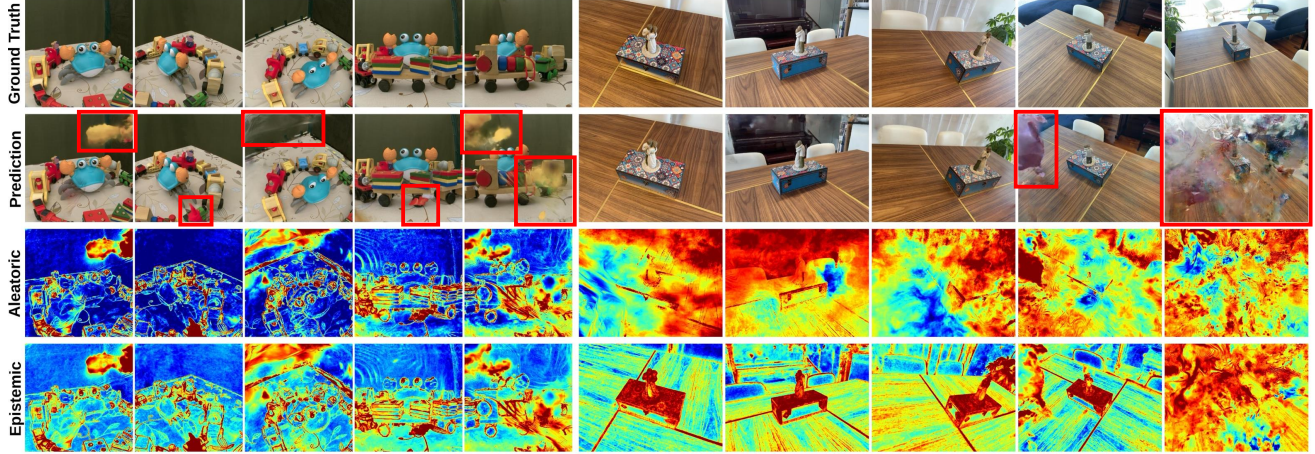


Figure 10. Aleatoric and epistemic uncertainties of scenes with transient objects. The red bounding boxes delineate the erroneous artifacts in test renderings caused by transients in the training views. If the model fails to suppress the floaters, both AU and EU are elevated on the transients; If the model resolves the transience, only AU is higher on the regions where the training transients were once present.

counterparts as specified in Equations (27) to (29). Conversely, if the density ρ_i were modeled as some random variable, not only would the variance of voxel weight $w_i = \exp\left(-\sum_{j=1}^{i-1} \rho_j \delta_j\right) (1 - \exp(-\rho_i \delta_i))$ be nontrivial to derive, but also the aleatoric and epistemic uncertainty aggregation formulae would be invalidated. This limitation leads to a failure mode on modeling transient objects. Although the current framework captures the color variation incurred by the transients, the corresponding density uncertainty is not effectively modeled, which is an important direction for future investigation.

Future directions. Future research directions include the following three aspects.

- Modeling density uncertainties. As previously discussed, incorporating density uncertainty into the evidential framework is nontrivial yet crucial for fully exploiting the potential of uncertainty modeling in dynamic 3D scenes.
- Generalizing to other radiance field frameworks. Although the current evidential framework is proposed for canonical NeRF, its direct compatibility with the volumetric rendering paradigm makes its extension to other 3D scene representations, such as Plenoxels and 3D Gaussian Splatting, highly feasible.
- Exploring downstream applications. While this paper focuses on the theoretical foundation, a crucial next step involves applying the evidential framework to practical real-world tasks, such as safety-critical robotics and autonomous driving.

Scene	Method	PSNR \uparrow	SSIM \uparrow	LPIPS \downarrow	NLL \downarrow	AUSE RMSE \downarrow	AUSE MAE \downarrow	AUCE \downarrow
Africa	Dropout	27.2231 ± 0.1780	0.9040 ± 0.0007	0.0537 ± 0.0009	6.9593 ± 0.4326	0.0140 ± 0.0002	0.0062 ± 0.0001	0.2474 ± 0.0032
	Normal	27.0908 ± 0.0423	0.9036 ± 0.0007	0.0532 ± 0.0003	-1.6826 ± 0.0160	0.0120 ± 0.0001	0.0062 ± 0.0000	0.1017 ± 0.0017
	MoL	26.9621 ± 0.0733	0.8806 ± 0.0014	0.0975 ± 0.0038	-1.3710 ± 0.0009	0.0220 ± 0.0013	0.0084 ± 0.0004	0.3258 ± 0.0151
	BayesRays	26.8235 ± 0.1644	0.9048 ± 0.0012	0.0541 ± 0.0008	0.6234 ± 0.0053	0.0442 ± 0.0024	0.0188 ± 0.0010	0.4736 ± 0.0002
	Ensembles	27.5923 ± 0.0757	0.9206 ± 0.0003	0.0420 ± 0.0003	0.5977 ± 0.2590	0.0071 ± 0.0003	0.0032 ± 0.0000	0.2051 ± 0.0013
	DANE	27.5923 ± 0.0757	0.9206 ± 0.0003	0.0420 ± 0.0003	-0.2229 ± 0.2434	0.0137 ± 0.0011	0.0057 ± 0.0003	0.0869 ± 0.0012
	Evidential	29.5031 ± 0.0846	0.9312 ± 0.0010	0.0384 ± 0.0038	-2.4190 ± 0.0281	0.0056 ± 0.0002	0.0028 ± 0.0001	0.1104 ± 0.0028
	Basket	Dropout	26.8884 ± 0.3224	0.8848 ± 0.0068	0.0690 ± 0.0042	10.2877 ± 0.5116	0.0168 ± 0.0003	0.0056 ± 0.0001
Normal		28.5171 ± 0.1327	0.9079 ± 0.0017	0.0511 ± 0.0007	-1.7838 ± 0.0283	0.0145 ± 0.0002	0.0066 ± 0.0000	0.1415 ± 0.0017
MoL		27.1461 ± 0.4038	0.8956 ± 0.0065	0.0951 ± 0.0081	-1.3766 ± 0.0103	0.0279 ± 0.0013	0.0096 ± 0.0004	0.3230 ± 0.0517
BayesRays		27.7572 ± 0.0634	0.9078 ± 0.0024	0.0578 ± 0.0011	0.6019 ± 0.0016	0.0405 ± 0.0004	0.0202 ± 0.0002	0.4739 ± 0.0003
Ensembles		28.7024 ± 0.0470	0.9228 ± 0.0004	0.0473 ± 0.0005	-0.2969 ± 0.0643	0.0055 ± 0.0002	0.0021 ± 0.0000	0.1748 ± 0.0039
DANE		28.7024 ± 0.0470	0.9228 ± 0.0004	0.0473 ± 0.0005	-0.4703 ± 0.0595	0.0070 ± 0.0006	0.0027 ± 0.0002	0.1297 ± 0.0131
Evidential		28.9140 ± 0.1662	0.9247 ± 0.0012	0.0347 ± 0.0010	-1.8512 ± 0.0109	0.0119 ± 0.0010	0.0038 ± 0.0002	0.1580 ± 0.0072
Statue		Dropout	31.6380 ± 0.1491	0.9539 ± 0.0014	0.0319 ± 0.0009	-0.4944 ± 0.1539	0.0060 ± 0.0003	0.0031 ± 0.0001
	Normal	29.3663 ± 0.0265	0.9420 ± 0.0003	0.0401 ± 0.0001	-2.1591 ± 0.0100	0.0059 ± 0.0001	0.0026 ± 0.0000	0.2010 ± 0.0007
	MoL	31.4981 ± 0.3223	0.9525 ± 0.0011	0.0474 ± 0.0006	-1.4769 ± 0.0010	0.0101 ± 0.0006	0.0029 ± 0.0001	0.4042 ± 0.0006
	BayesRays	32.3533 ± 0.0694	0.9640 ± 0.0003	0.0207 ± 0.0001	0.6233 ± 0.0020	0.0198 ± 0.0002	0.0097 ± 0.0000	0.4839 ± 0.0000
	Ensembles	33.2549 ± 0.1359	0.9707 ± 0.0005	0.0188 ± 0.0007	-1.0787 ± 0.0854	0.0027 ± 0.0001	0.0016 ± 0.0000	0.2136 ± 0.0041
	DANE	33.2549 ± 0.1359	0.9707 ± 0.0005	0.0188 ± 0.0007	-1.4183 ± 0.1692	0.0032 ± 0.0002	0.0018 ± 0.0001	0.1713 ± 0.0188
	Evidential	33.1178 ± 0.1144	0.9670 ± 0.0001	0.0204 ± 0.0006	-2.9394 ± 0.0036	0.0032 ± 0.0001	0.0015 ± 0.0000	0.0941 ± 0.0035
	Torch	Dropout	26.6079 ± 0.0730	0.8834 ± 0.0012	0.0697 ± 0.0000	5.7030 ± 0.5944	0.0138 ± 0.0001	0.0046 ± 0.0002
Normal		27.6167 ± 0.0346	0.9028 ± 0.0009	0.0611 ± 0.0006	-2.0509 ± 0.0061	0.0085 ± 0.0000	0.0038 ± 0.0001	0.1589 ± 0.0024
MoL		26.5564 ± 0.0791	0.8899 ± 0.0010	0.0675 ± 0.0022	-1.3432 ± 0.0043	0.0128 ± 0.0001	0.0034 ± 0.0002	0.1925 ± 0.0034
BayesRays		26.9788 ± 0.1539	0.8924 ± 0.0017	0.0602 ± 0.0016	0.6364 ± 0.0359	0.0432 ± 0.0026	0.0224 ± 0.0028	0.4724 ± 0.0003
Ensembles		27.7638 ± 0.0580	0.9086 ± 0.0005	0.0537 ± 0.0005	2.7548 ± 1.3789	0.0095 ± 0.0019	0.0025 ± 0.0002	0.1548 ± 0.0045
DANE		27.7638 ± 0.0580	0.9086 ± 0.0005	0.0537 ± 0.0005	1.5218 ± 1.6701	0.0153 ± 0.0011	0.0054 ± 0.0010	0.0912 ± 0.0011
Evidential		28.1922 ± 0.0515	0.9153 ± 0.0001	0.0481 ± 0.0007	-2.7217 ± 0.0336	0.0070 ± 0.0008	0.0022 ± 0.0003	0.0597 ± 0.0056

Table 4. Mean and standard deviation of quantitative metrics over three runs on LF.

Scene	Method	PSNR \uparrow	SSIM \uparrow	LPIPS \downarrow	NLL \downarrow	AUSE RMSE \downarrow	AUSE MAE \downarrow	AUCE \downarrow
Fern	Dropout	19.4680 ± 0.1659	0.5252 ± 0.0139	0.4323 ± 0.0221	43.9286 ± 2.9481	0.0495 ± 0.0023	0.0279 ± 0.0019	0.3719 ± 0.0053
	Normal	19.2266 ± 0.0624	0.5578 ± 0.0029	0.3384 ± 0.0021	5.4036 ± 0.0769	0.0477 ± 0.0005	0.0301 ± 0.0004	0.2586 ± 0.0016
	MoL	18.0732 ± 0.5043	0.5042 ± 0.0251	0.4400 ± 0.0327	1.7750 ± 0.6440	0.0687 ± 0.0084	0.0336 ± 0.0059	0.2871 ± 0.0177
	BayesRays	19.9116 ± 0.1128	0.5609 ± 0.0044	0.3692 ± 0.0028	3.6380 ± 0.0501	0.0818 ± 0.0007	0.0555 ± 0.0007	0.4882 ± 0.0001
	Ensembles	20.6844 ± 0.1179	0.6131 ± 0.0041	0.3464 ± 0.0029	3.3542 ± 0.4057	0.0296 ± 0.0005	0.0148 ± 0.0003	0.2416 ± 0.0062
	DANE	20.6844 ± 0.1179	0.6131 ± 0.0041	0.3464 ± 0.0029	2.7735 ± 0.3140	0.0333 ± 0.0003	0.0173 ± 0.0002	0.2078 ± 0.0059
	Evidential	20.8445 ± 0.1190	0.6252 ± 0.0046	0.3001 ± 0.0044	0.2397 ± 0.0206	0.0315 ± 0.0016	0.0174 ± 0.0011	0.3791 ± 0.0034
	Flower	Dropout	18.5000 ± 0.2353	0.4916 ± 0.0143	0.3823 ± 0.0049	54.1671 ± 1.3113	0.0559 ± 0.0016	0.0344 ± 0.0014
Normal		16.4914 ± 0.0117	0.4044 ± 0.0008	0.3968 ± 0.0031	14.0687 ± 0.3208	0.0803 ± 0.0015	0.0500 ± 0.0010	0.2822 ± 0.0017
MoL		17.9422 ± 0.0752	0.4857 ± 0.0077	0.4012 ± 0.0135	1.8365 ± 0.3830	0.0656 ± 0.0005	0.0340 ± 0.0005	0.2911 ± 0.0045
BayesRays		18.3437 ± 0.0780	0.4752 ± 0.0055	0.4291 ± 0.0113	4.1272 ± 0.0314	0.0732 ± 0.0010	0.0455 ± 0.0007	0.4891 ± 0.0000
Ensembles		18.7427 ± 0.0123	0.5176 ± 0.0017	0.4020 ± 0.0025	7.7557 ± 0.2685	0.0370 ± 0.0004	0.0173 ± 0.0001	0.2899 ± 0.0011
DANE		18.7427 ± 0.0123	0.5176 ± 0.0017	0.4020 ± 0.0025	7.7053 ± 0.2739	0.0372 ± 0.0003	0.0174 ± 0.0001	0.2888 ± 0.0012
Evidential		18.8858 ± 0.0187	0.5003 ± 0.0012	0.4348 ± 0.0053	0.3045 ± 0.0569	0.0476 ± 0.0010	0.0300 ± 0.0006	0.3281 ± 0.0069
Fortress		Dropout	18.3454 ± 0.5422	0.4099 ± 0.0036	0.5199 ± 0.0093	50.2036 ± 4.6159	0.0520 ± 0.0072	0.0279 ± 0.0022
	Normal	19.7801 ± 0.1042	0.3856 ± 0.0025	0.3586 ± 0.0072	4.1759 ± 0.3027	0.0353 ± 0.0007	0.0227 ± 0.0002	0.2428 ± 0.0006
	MoL	17.1176 ± 0.2163	0.3996 ± 0.0125	0.5810 ± 0.0280	8.1086 ± 8.1378	0.0763 ± 0.0014	0.0307 ± 0.0005	0.3201 ± 0.0055
	BayesRays	18.5904 ± 0.1161	0.3938 ± 0.0017	0.5093 ± 0.0051	3.8386 ± 0.0145	0.0803 ± 0.0003	0.0447 ± 0.0002	0.4885 ± 0.0001
	Ensembles	18.9232 ± 0.0149	0.4426 ± 0.0005	0.4543 ± 0.0034	6.9867 ± 0.1418	0.0360 ± 0.0003	0.0184 ± 0.0001	0.2848 ± 0.0016
	DANE	18.9232 ± 0.0149	0.4426 ± 0.0005	0.4543 ± 0.0034	6.5659 ± 0.0916	0.0368 ± 0.0004	0.0192 ± 0.0002	0.2717 ± 0.0013
	Evidential	19.1675 ± 0.2207	0.4374 ± 0.0043	0.4574 ± 0.0101	1.5399 ± 0.8732	0.0423 ± 0.0068	0.0210 ± 0.0025	0.3638 ± 0.0073
	Horns	Dropout	15.3957 ± 0.2979	0.4298 ± 0.0147	0.4700 ± 0.0114	164.8900 ± 22.7577	0.0945 ± 0.0066	0.0492 ± 0.0029
Normal		15.0760 ± 0.0487	0.3839 ± 0.0030	0.4511 ± 0.0026	14.5310 ± 0.3270	0.0868 ± 0.0004	0.0505 ± 0.0001	0.3001 ± 0.0020
MoL		14.3498 ± 0.0829	0.3663 ± 0.0295	0.5444 ± 0.0612	3.7191 ± 0.6307	0.1115 ± 0.0015	0.0542 ± 0.0019	0.3135 ± 0.0063
BayesRays		15.5735 ± 0.1586	0.4430 ± 0.0059	0.4544 ± 0.0045	3.8591 ± 0.0117	0.0995 ± 0.0011	0.0590 ± 0.0007	0.4884 ± 0.0001
Ensembles		16.0517 ± 0.0578	0.5028 ± 0.0026	0.4242 ± 0.0022	17.4362 ± 2.9944	0.0708 ± 0.0014	0.0313 ± 0.0004	0.2810 ± 0.0017
DANE		16.0517 ± 0.0578	0.5028 ± 0.0026	0.4242 ± 0.0022	13.0404 ± 0.7143	0.0699 ± 0.0010	0.0315 ± 0.0003	0.2746 ± 0.0015
Evidential		15.7414 ± 0.0358	0.5170 ± 0.0129	0.3770 ± 0.0177	3.1718 ± 0.2286	0.1036 ± 0.0023	0.0447 ± 0.0016	0.3833 ± 0.0098

Table 5. Mean and standard deviation of quantitative metrics over three runs on LLFF.

Scene	Method	PSNR \uparrow	SSIM \uparrow	LPIPS \downarrow	NLL \downarrow	AUSE RMSE \downarrow	AUSE MAE \downarrow	AUCE \downarrow
Leaves	Dropout	13.9939 ± 0.0600	0.2365 ± 0.0080	0.4269 ± 0.0038	145.2463 ± 9.5521	0.1065 ± 0.0009	0.0619 ± 0.0007	0.4191 ± 0.0003
	Normal	13.3483 ± 0.0185	0.2104 ± 0.0040	0.4216 ± 0.0021	14.8303 ± 0.1343	0.0801 ± 0.0007	0.0477 ± 0.0004	0.3408 ± 0.0006
	MoL	13.0330 ± 0.0760	0.2416 ± 0.0055	0.4147 ± 0.0062	3.3634 ± 0.3578	0.1159 ± 0.0019	0.0612 ± 0.0012	0.3058 ± 0.0034
	BayesRays	13.9149 ± 0.0858	0.2797 ± 0.0108	0.4040 ± 0.0090	3.5416 ± 0.0209	0.1640 ± 0.0007	0.1147 ± 0.0009	0.4851 ± 0.0002
	Ensembles	14.2332 ± 0.0762	0.2952 ± 0.0085	0.4339 ± 0.0048	12.3597 ± 0.8442	0.0916 ± 0.0014	0.0472 ± 0.0012	0.2780 ± 0.0011
	DANE	14.2332 ± 0.0762	0.2952 ± 0.0085	0.4339 ± 0.0048	11.7830 ± 0.6081	0.0928 ± 0.0015	0.0483 ± 0.0013	0.2752 ± 0.0011
	Evidential	13.9939 ± 0.0569	0.3006 ± 0.0023	0.3957 ± 0.0044	4.4300 ± 0.0229	0.0874 ± 0.0009	0.0455 ± 0.0006	0.3744 ± 0.0008
	Orchids	Dropout	13.2901 ± 0.3709	0.2139 ± 0.0185	0.4735 ± 0.0080	121.2939 ± 14.0288	0.1183 ± 0.0087	0.0755 ± 0.0057
Normal		12.8381 ± 0.0767	0.2006 ± 0.0035	0.4286 ± 0.0010	21.9843 ± 0.8903	0.1399 ± 0.0021	0.0986 ± 0.0019	0.3667 ± 0.0024
MoL		13.7039 ± 0.1631	0.3076 ± 0.0090	0.3672 ± 0.0050	3.0378 ± 0.2212	0.1091 ± 0.0037	0.0544 ± 0.0022	0.3092 ± 0.0059
BayesRays		14.4719 ± 0.0889	0.3014 ± 0.0068	0.3896 ± 0.0052	3.3730 ± 0.0149	0.1053 ± 0.0001	0.0664 ± 0.0003	0.4859 ± 0.0001
Ensembles		14.8121 ± 0.0152	0.3249 ± 0.0003	0.3941 ± 0.0009	10.4428 ± 0.3138	0.0774 ± 0.0009	0.0413 ± 0.0004	0.2995 ± 0.0008
DANE		14.8121 ± 0.0152	0.3249 ± 0.0003	0.3941 ± 0.0009	9.9662 ± 0.2237	0.0764 ± 0.0007	0.0410 ± 0.0003	0.2987 ± 0.0008
Evidential		14.4337 ± 0.1113	0.3150 ± 0.0020	0.3675 ± 0.0020	3.1018 ± 0.1056	0.0885 ± 0.0007	0.0476 ± 0.0006	0.4050 ± 0.0025
Room		Dropout	19.2386 ± 0.1170	0.6715 ± 0.0048	0.4505 ± 0.0042	87.3169 ± 10.4561	0.0634 ± 0.0012	0.0333 ± 0.0006
	Normal	18.3417 ± 0.0252	0.6361 ± 0.0078	0.4096 ± 0.0148	5.3266 ± 0.0167	0.0396 ± 0.0004	0.0235 ± 0.0002	0.2443 ± 0.0021
	MoL	17.9607 ± 0.2566	0.5943 ± 0.0592	0.5251 ± 0.0705	4.7781 ± 0.7674	0.0728 ± 0.0028	0.0353 ± 0.0027	0.3393 ± 0.0081
	BayesRays	19.6837 ± 0.0981	0.7164 ± 0.0059	0.3950 ± 0.0081	4.3263 ± 0.0129	0.0892 ± 0.0003	0.0541 ± 0.0004	0.4891 ± 0.0001
	Ensembles	19.9058 ± 0.0320	0.7492 ± 0.0024	0.3680 ± 0.0052	14.0229 ± 1.4143	0.0342 ± 0.0011	0.0159 ± 0.0006	0.3058 ± 0.0059
	DANE	19.9058 ± 0.0320	0.7492 ± 0.0024	0.3680 ± 0.0052	11.9512 ± 1.0730	0.0362 ± 0.0010	0.0172 ± 0.0006	0.2761 ± 0.0057
	Evidential	20.1343 ± 0.0919	0.7136 ± 0.0154	0.3736 ± 0.0253	0.5449 ± 0.1642	0.0404 ± 0.0037	0.0215 ± 0.0026	0.3435 ± 0.0288
	T-Rex	Dropout	19.0147 ± 0.1727	0.5702 ± 0.0083	0.4165 ± 0.0035	70.4616 ± 6.0129	0.0531 ± 0.0000	0.0288 ± 0.0005
Normal		17.1251 ± 0.1068	0.5057 ± 0.0036	0.4056 ± 0.0061	7.4545 ± 0.0449	0.0579 ± 0.0008	0.0327 ± 0.0003	0.2717 ± 0.0004
MoL		18.8802 ± 0.0643	0.6110 ± 0.0047	0.3549 ± 0.0070	2.6290 ± 0.8028	0.0541 ± 0.0024	0.0230 ± 0.0011	0.2941 ± 0.0131
BayesRays		19.7022 ± 0.0476	0.6049 ± 0.0055	0.3484 ± 0.0080	3.9710 ± 0.0210	0.0848 ± 0.0007	0.0563 ± 0.0006	0.4891 ± 0.0001
Ensembles		20.0225 ± 0.0199	0.6377 ± 0.0012	0.3309 ± 0.0019	11.9309 ± 0.5062	0.0296 ± 0.0006	0.0146 ± 0.0003	0.3239 ± 0.0010
DANE		20.0225 ± 0.0199	0.6377 ± 0.0012	0.3309 ± 0.0019	11.5491 ± 0.4599	0.0298 ± 0.0006	0.0147 ± 0.0003	0.3206 ± 0.0008
Evidential		19.8021 ± 0.0634	0.6323 ± 0.0062	0.3147 ± 0.0035	4.7364 ± 0.3272	0.0344 ± 0.0003	0.0170 ± 0.0002	0.3907 ± 0.0063

Table 6. Mean and standard deviation of quantitative metrics over three runs on LLFF.

Scene	Method	PSNR \uparrow	SSIM \uparrow	LPIPS \downarrow	NLL \downarrow	AUSE RMSE \downarrow	AUSE MAE \downarrow	AUCE \downarrow
Android	Dropout	22.5915 ± 0.1057	0.7525 ± 0.0009	0.1718 ± 0.0010	18.8141 ± 0.9535	0.0313 ± 0.0001	0.0191 ± 0.0002	0.3494 ± 0.0028
	Normal	23.0505 ± 0.0738	0.7866 ± 0.0030	0.1466 ± 0.0034	0.0427 ± 0.8648	0.0821 ± 0.0568	0.0660 ± 0.0471	0.2483 ± 0.0079
	MoL	21.8660 ± 0.0377	0.7268 ± 0.0027	0.2015 ± 0.0018	-0.7413 ± 0.0306	0.0295 ± 0.0008	0.0187 ± 0.0006	0.1800 ± 0.0016
	BayesRays	22.8201 ± 0.0860	0.7683 ± 0.0006	0.1558 ± 0.0006	0.4657 ± 0.0041	0.0500 ± 0.0018	0.0312 ± 0.0008	0.4370 ± 0.0006
	Ensembles	23.3925 ± 0.0309	0.8004 ± 0.0007	0.1394 ± 0.0006	7.8360 ± 0.4412	0.0263 ± 0.0001	0.0158 ± 0.0001	0.2947 ± 0.0022
	DANE	23.3925 ± 0.0309	0.8004 ± 0.0007	0.1394 ± 0.0006	7.1260 ± 0.4184	0.0271 ± 0.0001	0.0163 ± 0.0001	0.2572 ± 0.0024
	Evidential	23.6178 ± 0.0500	0.8062 ± 0.0008	0.1149 ± 0.0021	-0.2862 ± 0.0266	0.0345 ± 0.0001	0.0220 ± 0.0001	0.2175 ± 0.0062
	Crab	Dropout	27.8252 ± 0.4488	0.8882 ± 0.0044	0.1141 ± 0.0049	22.2539 ± 6.6734	0.0198 ± 0.0025	0.0069 ± 0.0006
Normal		29.2132 ± 0.1981	0.9096 ± 0.0021	0.0914 ± 0.0005	7.4096 ± 1.8880	0.0193 ± 0.0033	0.0069 ± 0.0013	0.1045 ± 0.0076
MoL		25.8615 ± 0.4790	0.8466 ± 0.0140	0.1786 ± 0.0200	-2.0644 ± 0.2296	0.0321 ± 0.0056	0.0151 ± 0.0043	0.0861 ± 0.0125
BayesRays		28.4892 ± 0.2354	0.8994 ± 0.0035	0.1139 ± 0.0054	0.0470 ± 0.0157	0.0224 ± 0.0012	0.0081 ± 0.0004	0.4628 ± 0.0010
Ensembles		29.9028 ± 0.0546	0.9213 ± 0.0003	0.1055 ± 0.0006	0.5184 ± 0.2531	0.0047 ± 0.0001	0.0021 ± 0.0000	0.1929 ± 0.0067
DANE		29.9028 ± 0.0546	0.9213 ± 0.0003	0.1055 ± 0.0006	0.1598 ± 0.0376	0.0241 ± 0.0005	0.0104 ± 0.0001	0.1418 ± 0.0008
Evidential		29.7575 ± 0.4037	0.9151 ± 0.0036	0.0839 ± 0.0045	-2.3681 ± 0.1088	0.0127 ± 0.0031	0.0053 ± 0.0013	0.1122 ± 0.0099
Statue		Dropout	20.0992 ± 0.0570	0.7225 ± 0.0043	0.2730 ± 0.0065	33.5356 ± 1.1860	0.0458 ± 0.0005	0.0303 ± 0.0006
	Normal	20.3593 ± 0.0347	0.7753 ± 0.0017	0.2218 ± 0.0026	20.4344 ± 6.6918	0.0409 ± 0.0004	0.0269 ± 0.0004	0.3011 ± 0.0048
	MoL	19.4220 ± 0.0626	0.6913 ± 0.0033	0.3112 ± 0.0013	-0.1722 ± 0.0800	0.0567 ± 0.0033	0.0371 ± 0.0022	0.1918 ± 0.0041
	BayesRays	20.1634 ± 0.0965	0.7450 ± 0.0026	0.2418 ± 0.0053	0.4821 ± 0.0024	0.0709 ± 0.0008	0.0463 ± 0.0009	0.4061 ± 0.0029
	Ensembles	20.6510 ± 0.0240	0.7873 ± 0.0008	0.2111 ± 0.0021	10.3638 ± 0.1372	0.0298 ± 0.0002	0.0193 ± 0.0002	0.3172 ± 0.0024
	DANE	20.6510 ± 0.0240	0.7873 ± 0.0008	0.2111 ± 0.0021	8.8396 ± 0.1485	0.0367 ± 0.0002	0.0236 ± 0.0002	0.2297 ± 0.0028
	Evidential	20.4093 ± 0.0235	0.7819 ± 0.0023	0.2070 ± 0.0042	-0.2045 ± 0.0129	0.0405 ± 0.0014	0.0273 ± 0.0007	0.2957 ± 0.0045
	Yoda	Dropout	28.8179 ± 0.3366	0.8861 ± 0.0034	0.1325 ± 0.0075	15.5430 ± 4.9756	0.0155 ± 0.0024	0.0078 ± 0.0009
Normal		29.2424 ± 0.4484	0.9145 ± 0.0022	0.0950 ± 0.0055	12.9013 ± 6.4719	0.0213 ± 0.0045	0.0089 ± 0.0017	0.1567 ± 0.0020
MoL		26.9425 ± 0.1651	0.8630 ± 0.0041	0.1707 ± 0.0076	-2.1254 ± 0.0517	0.0232 ± 0.0023	0.0108 ± 0.0011	0.0963 ± 0.0021
BayesRays		30.3519 ± 0.1949	0.9073 ± 0.0073	0.1120 ± 0.0086	-0.0009 ± 0.0105	0.0212 ± 0.0014	0.0082 ± 0.0006	0.4632 ± 0.0021
Ensembles		30.9714 ± 0.2856	0.9230 ± 0.0012	0.1047 ± 0.0018	0.8007 ± 0.4480	0.0042 ± 0.0001	0.0019 ± 0.0000	0.2057 ± 0.0045
DANE		30.9714 ± 0.2856	0.9230 ± 0.0012	0.1047 ± 0.0018	0.4312 ± 0.1199	0.0227 ± 0.0011	0.0104 ± 0.0005	0.1380 ± 0.0007
Evidential		29.6492 ± 0.0817	0.9306 ± 0.0035	0.0724 ± 0.0046	-2.4270 ± 0.0133	0.0185 ± 0.0033	0.0105 ± 0.0011	0.1842 ± 0.0080

Table 7. Mean and standard deviation of quantitative metrics over three runs on RobustNeRF.

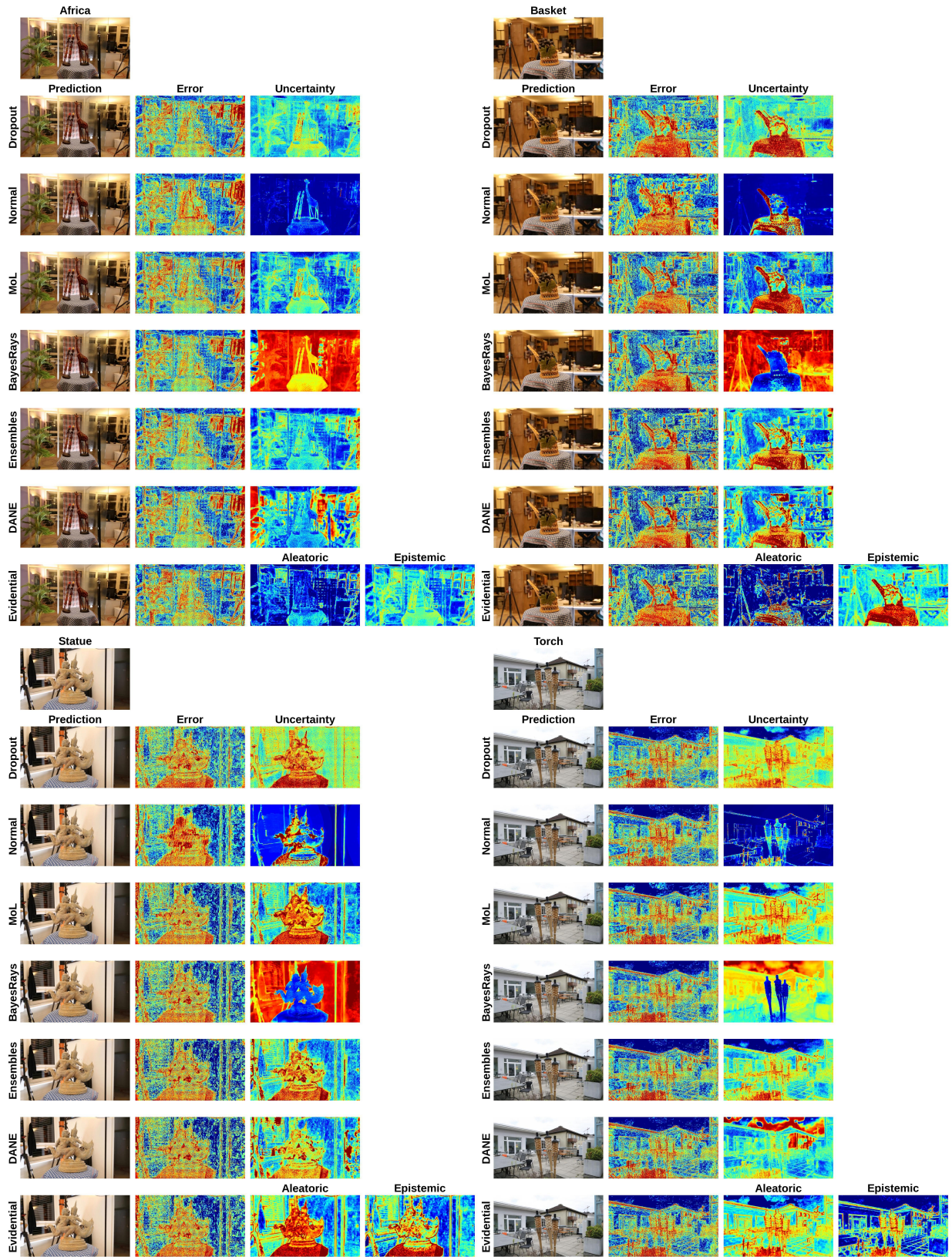


Figure 11. Qualitative comparison on LF.

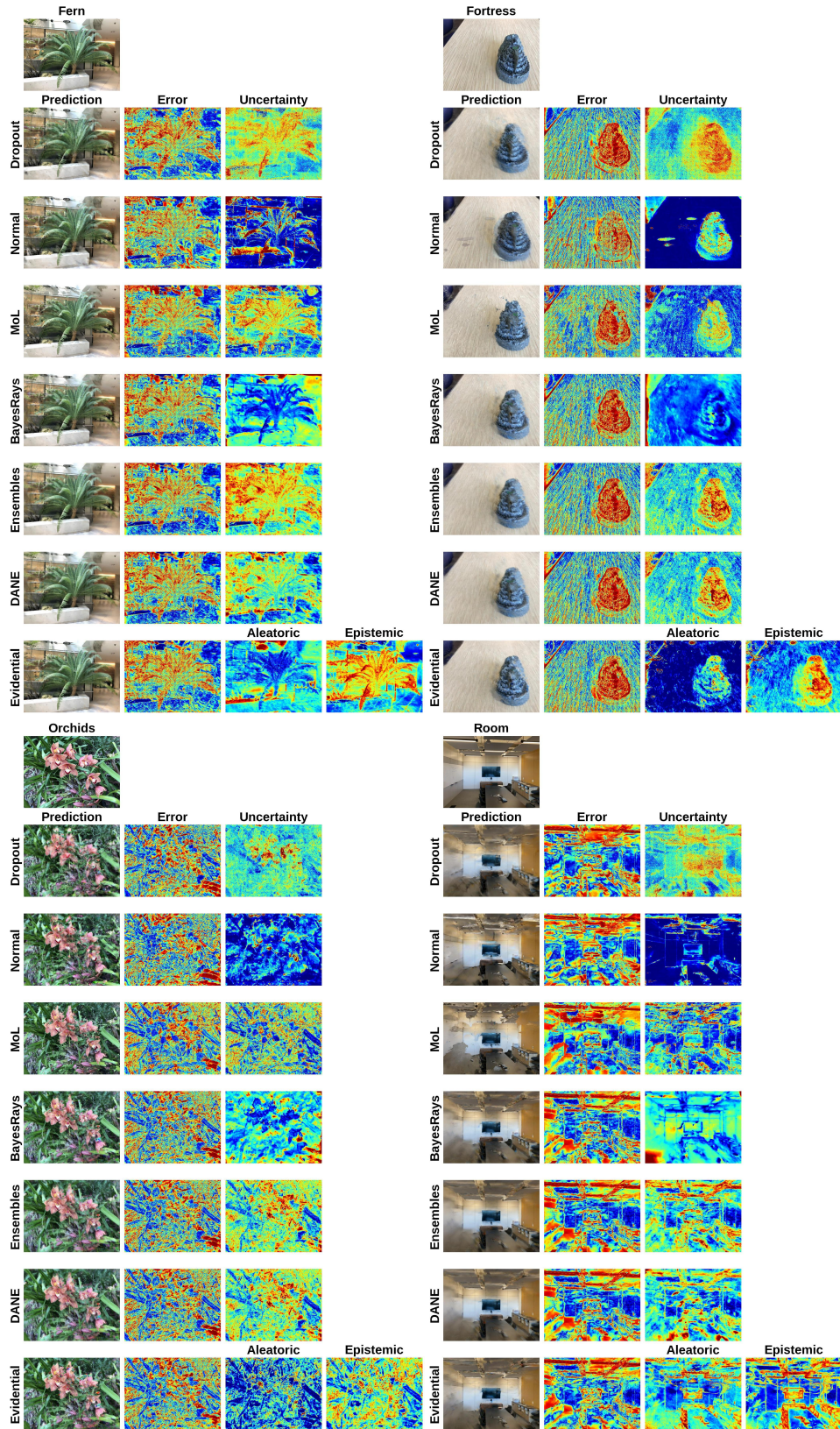


Figure 12. Qualitative comparison on LLFF.

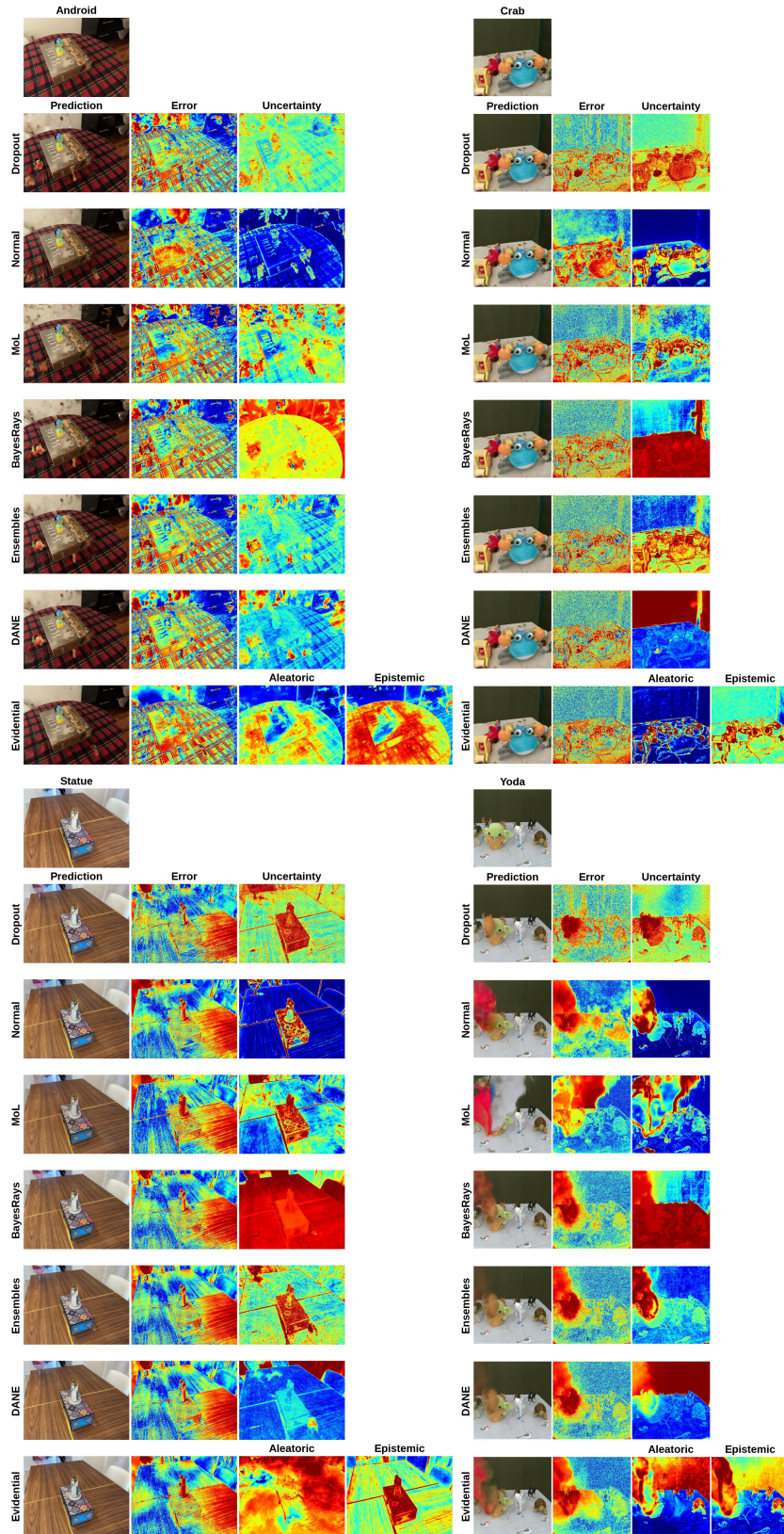


Figure 13. Qualitative comparison on RobustNeRF.

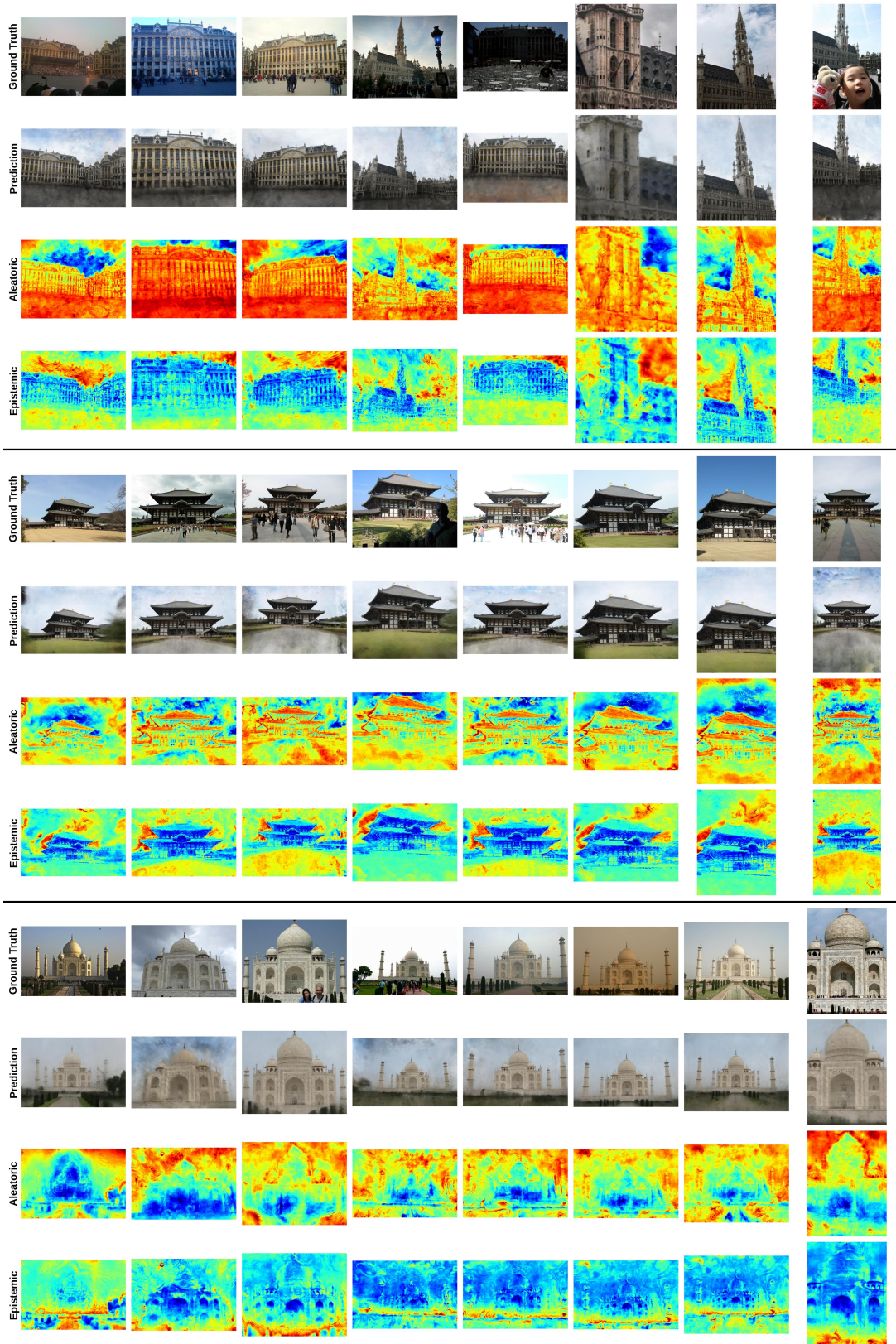


Figure 14. Aleatoric and epistemic uncertainty maps for three in-the-wild scenes from Phototourism. Aleatoric uncertainty peaks in regions with high radiance variance (e.g., sky higher above, building facades, moving figures), whereas epistemic uncertainty is concentrated in areas frequently occluded (e.g., sky directly behind the buildings or objects obscured by pedestrians).